Supporting Information for "Lunar Gravitational Maps From GRAIL Gravity, LRO and Kaguya Topography and 3D Crustal Density"

Blažej Bucha[1]

[1]Department of Theoretical Geodesy and Geoinformatics, Slovak University of Technology in Bratislava, Radlinského 11, 81005 Bratislava, Slovak Republic

Contents of this file

1. Text S1 to S5
2. Figures S1 to S17
3. Tables S1 to S8

Introduction

Lunar Gravitational Maps 2026 (LGM2026) show the gravitational field of the Moon at the spatial resolution of 128 pixels per degree (PPD), which corresponds to ∼250 m at the equator. The gravitational field is mapped at the lunar surface and on its minimum circumscribing sphere using the gravitational potential, the gravitational vector and the

Corresponding author: B. Bucha, Department of Theoretical Geodesy and Geoinformatics, Slovak University of Technology in Bratislava, Radlinského 11, 81005 Bratislava, Slovak Republic. (blazej.bucha@stuba.sk)

gravitational tensor. LGM2026 combines gravitational data observed by the Gravity Recovery and Interior Laboratory mission (GRAIL; Zuber et al., 2013) with the gravitational field forward-modeled from topography and 3D crustal density model. The topography was represented by the lunar shape model LDEM128_PA_pixel_202405 (briefly LDEM128; Neumann, 2024) from the Lunar Reconnaissance Orbiter (LRO; Chin et al., 2007) and Kaguya missions (Kato et al., 2010). The linear 3D density model with the cap radius of 15° and degree range 250–650 by Goossens et al. (2020) was use to represent the crustal density. LGM2026 can be beneficial for applications seeking accurate gravitational information at small spatial scales such as spacecraft navigation at landing sites, inertial navigation or the establishment of a physically meaningful height system. Given that the short-scale signals (beyond spherical-harmonic degree 500, less than ∼11 km at the equator) do not rely on observed gravitational data but instead are modeled from topography, they must not be geophysically interpreted.

This Supporting Information describes the methodology behind LGM2026 (Text S1), the key concepts of the involved gravity-forward modeling methods (Text S2), empirical choices made during the LGM2026 development (Text S3), the low-frequency correction of the residual terrain modeling technique (Text S4) and the validation of LGM2026 (Text S5).

Text S1. Methodology

LGM2026 builds on the principles that have been in use in Earth's gravity field modeling for 4 decades and thus are well established by now. The key idea is to take long-wavelength gravity from GRAIL satellite observations and combine it with short-scale gravity implied

by near-surface lunar topographic masses. Specific to LGM2026 is the use of a 3D variable crustal density model and the calculation of the gravitational contribution of the topography by a spectral technique with spatially restricted integration domain.

Text S1.1. LGM2026 overview

LGM2026 maps show the gravitational potential V, the gravitational vector

$$\vec{g} = \nabla V = \begin{bmatrix} V^{\mathrm{x}} \\ V^{\mathrm{y}} \\ V^{\mathrm{z}} \end{bmatrix} \tag{1}$$

and the gravitational tensor

$$\mathbf{V} = \nabla \otimes \nabla V = \begin{bmatrix} V^{\mathrm{xx}} & V^{\mathrm{xy}} & V^{\mathrm{xz}} \\ V^{\mathrm{yx}} & V^{\mathrm{yy}} & V^{\mathrm{yz}} \\ V^{\mathrm{zx}} & V^{\mathrm{zy}} & V^{\mathrm{zz}} \end{bmatrix}. \tag{2}$$

The gravitational vector and tensor are expressed in the local north-oriented reference frame (LNOF), which is a right-handed Cartesian coordinate system with the origin at the evaluation point, the x-axis pointing to the north, the y-axis pointing to the west and the z-axis pointing radially outwards. All quantities are provided 0.1 m above the lunar topography as represented by LDEM128 (briefly at the topography; see Figures S1, S2, S3, S4) and on the sphere of the radius 1749 km passing outside lunar masses (briefly on the circumscribing sphere; see Figures S5, S6, S7, S8). Neither the centrifugal field nor the normal gravity field are included in LGM2026. Given that the 3D position of the LGM2026 points is published along with the maps, these contributions can readily be evaluated whenever necessary.

All LGM2026 quantities, V, $\vec{g}$ and $\mathbf{V}$, were computed in the same manner, so we shall demonstrate the development strategy using the gravitational potential V only. The

gravitational potential V was obtained as

$$V = V^{\mathrm{GRAIL}} + V^{\mathrm{RTM}}, \tag{3}$$

where V^{GRAIL} is the long-wavelength component from the Kaula-constrained GRAIL-based spherical-harmonic model GRGM1200B (Goossens et al., 2020) up to degree 500 (Text S1.2) and V^{RTM} is the high-frequency component derived from the topography using residual terrain modeling (RTM; Text S1.3).

Text S1.2. Long-wavelength component

The V^{GRAIL} term from Equation (3) relies on observed GRAIL gravitational data through the Kaula-constrained GRGM1200B model (briefly GRGM1200B). This model was derived from the primary and extended GRAIL mission data and contains spherical-harmonic coefficients of the lunar external gravitational field up to degree 1200.

The long-wavelength component V^{GRAIL} was obtained by the solid spherical-harmonic synthesis of the $\bar{V}_{nm}^{\mathrm{GRAIL}}$ coefficients from GRGM1200B up to degree 500 using the relation

$$V^{\mathrm{GRAIL}}(r,\varphi,\lambda) = \frac{\mathrm{GM}^{\mathrm{GRAIL}}}{R^{\mathrm{GRAIL}}} \sum_{n=0}^{500} \left(\frac{R^{\mathrm{GRAIL}}}{r}\right)^{n+1} \sum_{m=-n}^{n} \bar{V}_{nm}^{\mathrm{GRAIL}}\, \bar{Y}_{nm}(\varphi,\lambda), \tag{4}$$

where r, φ, λ are the spherical radius, the spherical latitude and the spherical longitude of evaluation points, $\mathrm{GM}^{\mathrm{GRAIL}}$ is the product of Newton's gravitational constant and mass of the Moon, R^{GRAIL} is the radius of the reference lunar sphere and $\bar{Y}_{nm}(\varphi,\lambda)$ are the 4π-fully normalized surface spherical harmonics. Note that $\mathrm{GM}^{\mathrm{GRAIL}}$ and R^{GRAIL} are scaling constants tied to GRGM1200B. Since GRGM1200B does not specify the zero-degree term $\bar{V}_{00}^{\mathrm{GRAIL}}$, we set it to 1, so that the dominant monopole component reads $\mathrm{GM}^{\mathrm{GRAIL}}/r$. The rationale behind the truncation degree 500 will be discussed in Text S3.1.

Given the low truncation degree of 500, we used the exact algorithm for solid synthesis both at the lunar surface and on its circumscribing sphere, avoiding the more efficient but approximate gradient approach (e.g., Balmino et al., 2012; Hirt, 2012). To this end, we used CHarm, a C/Python library for spherical-harmonic transforms in planetary geodesy (Bucha, 2022). The evaluation of Equation (4) was parallelized using OpenMP and AVX2.

Text S1.3. Short-scale component

The high-frequency component V^{RTM} from Equation (3) was modeled from topography, leveraging the strong correlation between the lunar gravity and topography at small spatial scales (e.g., Zuber et al., 2013). The lunar topography beyond degree 500 is assumed to be isostatically uncompensated which seems realistic (e.g., Wieczorek et al., 2013).

RTM (e.g., Forsberg & Tscherning, 1981; Rexer et al., 2018; Hirt, Bucha, et al., 2019) evaluates short-scale gravitational features implied by topography using some gravity-forward modeling method. It relies on the concept of a residual topography (here abbreviated to LDEM128_RES), which is the difference between a high-resolution topography (here LDEM128) and its low-pass filtered spherical-harmonic representation (here Moon_LDEM128_shape_pa_11519.sh.gz, briefly LDEM128_SH; Wieczorek, 2024). Since LDEM128_SH was derived directly from LDEM128 (see Wieczorek, 2024), the consistency between LDEM128 and LDEM128_SH is guaranteed which is crucial for RTM (Hirt et al., 2014). By truncating LDEM128_SH at the same degree as GRGM1200B, that is, at degree 500, the gravitational field implied by the residual topography LDEM128_RES will contain mostly short-scale gravitational signals that are not captured by GRGM1200B up to degree 500. Thus, RTM can supplement gravitational signals beyond GRGM1200B

using lunar topography and density data. In Earth's gravity field modeling, numerous researchers have proved that RTM significantly enhances spherical-harmonic-based gravity models, in some cases by as much as 80 % (e.g., Hirt et al., 2013; Ďuríčková & Janák, 2016; Grombein et al., 2017). Importantly, the low- and high-frequency corrections as introduced by Rexer et al. (2018) must be applied to ensure proper RTM filtering as will be discussed below.

Let us assume that LDEM128 and LDEM128_SH were referenced to an internal sphere of the radius 1727 km, so that all heights are positive. Furthermore, let us formally denote by $\mathcal{G}(\text{DEM})$ the process of evaluating some functional of the gravitational potential that is generated by a digital elevation model DEM. This process is often called gravity-forward modeling or gravity-from-topography modeling. The type of the density model (constant, lateral, 3D, etc.) is not reflected by the notation, because it is irrelevant for our demonstration purposes as long as the density model is kept the same throughout the RTM modeling.

Schematically, our RTM modeling reads

$$V^{\text{RTM}} = \mathcal{G}^{T,\psi<180^\circ}_{0..\infty}(\text{LDEM128}_{0..\infty}) - \mathcal{G}^{\text{SH},\psi<180^\circ}_{0..500}(\text{LDEM128\_SH}_{0..500}) - \text{LF}. \tag{5}$$

Here, the subscripts indicate the spectral content. For instance, $\text{LDEM128\_SH}_{0..500}$ means that LDEM128_SH is expanded from degree 0 up to degree 500, $\mathcal{G}_{0..500}$ means that the gravitational effects from gravity-forward modeling are considered from degree 0 to 500 and so on. The first superscript next to $\mathcal{G}$ denotes gravity-forward modeling method: $\mathcal{G}^{\text{T}}$ stands for the spatial-domain method based on tesseroids due to Lin, Denker, and Müller (2020) (Text S2.1) and $\mathcal{G}^{\text{SH}}$ denotes the spherical-harmonic-based method of Bucha

(2025) (Text S2.2). The second superscript next to $\mathcal{G}$ uses the spherical distance ψ between the evaluation point and topographic masses to indicate masses that are gravity-forward modeled: $\psi < 180°$ therefore implies that all masses are integrated (global integration). Finally, LF in Equation (5) stands for the low-frequency correction, which will be discussed in Text S1.3.2.

Global spatial-domain gravity-forward modeling $\mathcal{G}_{0..\infty}^{T,\psi<180°}$ is computationally challenging due to the convolutional character of Newton's integral. Opposed to this, spectral spherical-harmonic-based methods, here denoted as $\mathcal{G}^{\mathrm{SH}}$, are orders of magnitude faster due to the underlying FFT. However, $\mathcal{G}^{\mathrm{SH},\psi<180°}$ usually cannot be used at the topography due to the divergence of spherical harmonics (Sansò, 2013). Recently, Bucha (2025) proposed a combined spatial-spectral method that works even at the topography. It integrates near-zone masses up to some ψ_0 (here $\psi_0 = 10°$) by a spatial-domain method (here $\mathcal{G}^T$) and the remaining masses beyond ψ_0 by a modification of the spectral method after Bucha (2025) (here $\mathcal{G}^{\mathrm{SH}}$). Bucha and Kuhn (2020) suggest that the spherical-harmonic-based method converges even at the topography as long as integrated are only far-zone masses with sufficiently large distance from evaluation points. According to Equation (15) of Bucha and Kuhn (2020), ψ_0 should be larger than $\psi_{\mathrm{conv}} = \max(\mathrm{LDEM128})/1727\ \mathrm{km} = 0.7°$ to achieve convergence everywhere at the lunar topography. To develop LGM2026, we used $\psi_0 = 10° > \psi_{\mathrm{conv}}$. Let us acknowledge that a formal proof of the hypothesis by Bucha and Kuhn (2020) has still not been found, but their numerical experiments and also those from this paper (Text S3.2) are consistent with the hypothesis.

Thus, too improve performance, the first term on the right-hand side of Equation (5) can be approximated as

$$\begin{aligned} \mathcal{G}_{0..\infty}^{T,\psi<180^\circ}(\mathrm{LDEM128}_{0..\infty}) &= \mathcal{G}_{0..\infty}^{T,\psi<10^\circ}(\mathrm{LDEM128}_{0..\infty}) + \mathcal{G}_{0..\infty}^{T,\psi\geq10^\circ}(\mathrm{LDEM128}_{0..\infty}) \\ &\approx \mathcal{G}_{0..\infty}^{T,\psi<10^\circ}(\mathrm{LDEM128}_{0..\infty}) + \mathcal{G}_{0..10800}^{\mathrm{SH},\psi\geq10^\circ}(\mathrm{LDEM128\_SH}_{0..5400}), \end{aligned} \tag{6}$$

where the notation $\psi < 10^\circ$ and $\psi \geq 10^\circ$ means that integrated are only masses up to and beyond the spherical distance $\psi_0 = 10^\circ$ from each evaluation point, respectively. The final RTM formula used to develop LGM2026 therefore reads

$$\begin{aligned} V^{\mathrm{RTM}} &= \mathcal{G}_{0..\infty}^{T,\psi<10^\circ}(\mathrm{LDEM128}_{0..\infty}) + \mathcal{G}_{0..10800}^{\mathrm{SH},\psi\geq10^\circ}(\mathrm{LDEM128\_SH}_{0..5400}) \\ &\quad - \mathcal{G}_{0..500}^{\mathrm{SH},\psi<180^\circ}(\mathrm{LDEM128\_SH}_{0..500}) - \mathrm{LF}. \end{aligned} \tag{7}$$

Let us remind that topography band-limited to degree $N > 0$ generates full-spectrum gravity field and that this holds for both spatial- and spectral-domain gravity-forward modeling methods (Hirt & Kuhn, 2014). This means that the gravity field of, say, $\mathrm{LDEM128\_SH}_{0..5400}$ covers all harmonics so that $\mathcal{G}_{0..\infty}^{\mathrm{SH},\psi<180^\circ}(\mathrm{LDEM128\_SH}_{0..5400}) = \mathcal{G}_{0..\infty}^{\mathrm{T},\psi<180^\circ}(\mathrm{LDEM128\_SH}_{0..5400})$ (for now, we assume evaluation points above the minimum lunar circumscribing sphere, so that $\mathcal{G}_{0..\infty}^{\mathrm{SH},\psi<180^\circ}$ converges). With spectral methods, it can thus be truncated at degree 10,800 as $\mathcal{G}_{0..10800}^{\mathrm{SH},\psi<180^\circ}(\mathrm{LDEM128\_SH}_{0..5400})$ (see Equation 7).

Text S1.3.1 High-frequency RTM correction

Our RTM modeling generally follows the baseline technique of Hirt, Bucha, et al. (2019). One of the differences between Hirt, Bucha, et al. (2019) and our Equation (7) is that Equation (7) does not include a high-frequency RTM correction term, which is defined as $\mathrm{HF} = \mathcal{G}_{501..\infty}^{\mathrm{SH},\psi<180^\circ}(\mathrm{LDEM128\_SH}_{0..500})$ (see Rexer et al., 2018). In our case, this cor-

rection must not be applied, because it is already accounted for by truncating the gravitational effects $\mathcal{G}_{0..500}^{\mathrm{SH},\psi<180^\circ}(\mathrm{LDEM128\_SH}_{0..500})$ at the desired degree of 500. The high-frequency correction is typically required when the gravitational field of $\mathrm{LDEM128\_SH}_{0..500}$ is evaluated by spatial-domain methods (e.g., prisms or tesseroids), which do not permit the spectral truncation of gravitational effects.

Text S1.3.2 Low-frequency RTM correction

Another difference between our RTM and that of Hirt, Bucha, et al. (2019) is that we took into account also the low-frequency correction (see LF in Equation 7; the study of Hirt, Bucha, et al. (2019) did not require this correction). The purpose of the low-frequency correction is to remove residual signals that are otherwise found in RTM below the resolution of the spherical-harmonic topography (here degrees up to 500; Rexer et al., 2018). After applying the correction, RTM does not contain any signal power up to degree 500, so that adding RTM to GRGM1200B (Equation 3) will not tamper the observed GRAIL signals found in GRGM1200B. We discuss 2 methods to compute the low-frequency RTM correction.

The method A reads in our notation

$$\begin{aligned}\mathrm{LF} &= \mathcal{G}_{0..500}^{\mathrm{SH},\psi<180^\circ}(\mathrm{LDEM128}_{0..\infty}) - \mathcal{G}_{0..500}^{\mathrm{SH},\psi<180^\circ}(\mathrm{LDEM128\_SH}_{0..500}) \\ &\approx \mathcal{G}_{0..500}^{\mathrm{SH},\psi<180^\circ}(\mathrm{LDEM128\_SH}_{0..5400}) - \mathcal{G}_{0..500}^{\mathrm{SH},\psi<180^\circ}(\mathrm{LDEM128\_SH}_{0..500}). \qquad (8)\end{aligned}$$

That is, the correction represents gravitational signals up to degree 500 which are implied by the residual topography. Clearly, substituting the relation after the equal sign in

Equation (8) into (5) leads to

$$V^{\text{RTM}} = \mathcal{G}_{0..\infty}^{T,\psi<180^\circ}(\text{LDEM128}_{0..\infty}) - \mathcal{G}_{0..500}^{\text{SH},\psi<180^\circ}(\text{LDEM128}_{0..\infty}), \tag{9}$$

which is the sought filtration of the gravitational effects implied by the high-resolution topography LDEM128. To our knowledge, this is a novel proof showing that the topography-implied gravity can be high-pass filtered exactly also by means of a reference spherical-harmonic topography as long as the low- and high-frequency corrections are applied. The obvious problem is that if N_T and N_G are too high in $\mathcal{G}_{0..N_G}^{\text{SH},\psi<180^\circ}(\text{LDEM128\_SH}_{0..N_T})$, convergence of the spherical-harmonic expansion of the gravitational potential is not guaranteed at the planetary surface. In fact, for realistic bodies and sufficiently high N_T and N_G, the series will likely diverge on the planetary body as shown numerous times in the literature (Hu & Jekeli, 2015; Hirt & Kuhn, 2017; Bucha & Sansò, 2021). In our case, $N_T = N_G = 500$ are sufficiently low and thus avoid the divergence of spherical harmonics at the lunar surface (see also Text S3.1).

A different approach, hereafter named the method B, was used by Rexer et al. (2018). It consists of 2 steps: (a) the spherical-harmonic analysis of

$$\begin{aligned} V^{\text{RTM without LF}} = {} & \mathcal{G}_{0..\infty}^{T,\psi<10^\circ}(\text{LDEM128}_{0..\infty}) + \mathcal{G}_{0..10800}^{\text{SH},\psi\geq10^\circ}(\text{LDEM128\_SH}_{0..5400}) \\ & - \mathcal{G}_{0..500}^{\text{SH},\psi<180^\circ}(\text{LDEM128\_SH}_{0..500}), \end{aligned} \tag{10}$$

where $V^{\text{RTM without LF}}$ is evaluated on a circumscribing sphere passing outside all masses, and (b) the synthesis of the obtained coefficients up to degree 500.

We shall numerically show in Text S4 that both approaches are equivalent. For reasons to be explained later in Text S4, we opted for the method B in the LGM2026 development.

Text S2. Gravity-forward modeling

Two gravity-forward modeling techniques were used to compute Equation (7): a spatial-domain technique based on tesseroids (Text S2.1) and a spectral-domain technique based on spherical harmonics (Text S2.2).

Text S2.1. Spatial-domain gravity-forward modeling

We used the tesseroid-based spatial-domain method of Lin et al. (2020) to evaluate $\mathcal{G}_{0..\infty}^{T,\psi<10^\circ}(\mathrm{LDEM128}_{0..\infty})$ from Equation (7). It calculates the gravitational potential, the gravitational vector and the gravitational tensor of a tesseroid, whose density $\rho(r')$ varies radially with r' as a finite-degree polynomial

$$\rho(r') = \sum_{i=0}^{I} \rho_i \, (r')^i. \tag{11}$$

Once the polynomial density coefficients ρ_i are allowed to vary with latitude φ' and longitude λ', that is, from tesseroid to tesseroid, gravity-forward modeling of lunar topography with 3D variable density is possible.

To represent the density, we used the $1^\circ \times 1^\circ$ linear 3D density model by Goossens et al. (2020) with the cap radius of 15° and degree range 250–650. This model provides the surface density $\rho_{\mathrm{surf}}(\varphi', \lambda')$ and its first-order gradient $\rho_{\mathrm{grad}}(\varphi', \lambda')$, so that the density is modeled as

$$\rho(r', \varphi', \lambda') = \rho_{\mathrm{surf}}(\varphi', \lambda') + \rho_{\mathrm{grad}}(\varphi', \lambda') \, z(r', \varphi', \lambda') \tag{12}$$

where $z(r', \varphi', \lambda') = r_{\mathrm{surf}}(\varphi', \lambda') - r'$ is the depth with respect to the lunar surface $r_{\mathrm{surf}}(\varphi', \lambda')$. By a simple transformation, the polynomial density coefficients from

Equation (11) are obtained as

$$\rho_0(\varphi', \lambda') = \rho_{\text{surf}}(\varphi', \lambda') + \rho_{\text{grad}}(\varphi', \lambda')\, r_{\text{surf}}(\varphi', \lambda') \tag{13}$$

and

$$\rho_1(\varphi', \lambda') = -\rho_{\text{grad}}(\varphi', \lambda'). \tag{14}$$

With the linear density model of Goossens et al. (2020), the order of the radial polynomial density coefficients is

$$I = 1. \tag{15}$$

Since density data in the model of Goossens et al. (2020) are missing near the poles (latitudes $|\varphi| \geq 88°$), we used the nearest neighbor interpolation to fill-in the gaps.

The method of Lin et al. (2020) evaluates Newton integral and its derivatives by the Gauss–Legendre quadrature in latitude, longitude and spherical radius. In all 3 dimensions, we used 11 quadrature nodes for all tesseroids up to $\psi < 0.3°$, 5 quadrature points for tesseroids with $0.3° \leq \psi < 0.5°$, 3 quadrature points if $0.5° \leq \psi < 3°$ and finally 2 quadrature points for $3° \leq \psi < 10°$. We found this setup to be a good compromise between the accuracy (see Text S5.4) and computing speed. The parameter related to the 2D adaptive subdivision was 10. The adopted value of Newton's gravitational constant is $G = 6.67430 \times 10^{-11}$ m^3 kg^{-1} s^{-2} (Tiesinga et al., 2021).

For reasons of numerical efficiency, the forward modeling $\mathcal{G}_{0..\infty}^{T,\psi<10°}(\text{LDEM128}_{0..\infty})$ was performed by combining 2 grids of different resolutions. We used LDEM128 sampled at 128 PPD for all tesseroids with spherical distance $\psi < 0.5°$ from evaluation points. At spherical distances $0.5° \leq \psi < 10°$, we used LDEM128 re-sampled to 64 PPD. This grid

was obtained from the original LDEM128 by a weighted block averaging, with weights being given by the pixel size.

Our implementation of the tesseroid-based technique is written the C programming language and employs OpenMP and AVX-512 parallelization techniques to efficiently tackle large-scale forward modeling tasks.

Text S2.2. Spectral-domain gravity-forward modeling

The $\mathcal{G}_{0..500}^{\mathrm{SH},\psi<180^\circ}(\mathrm{LDEM128\_SH}_{0..500})$ and $\mathcal{G}_{0..10800}^{\mathrm{SH},\psi\geq10^\circ}(\mathrm{LDEM128\_SH}_{0..5400})$ terms from Equation (7) were evaluated by the spherical-harmonic-based gravity-forward modeling technique of Bucha (2025), which is designed to work with constant, lateral and 3D density models. The method was developed for the gravitational potential, the gravitational vector and the gravitational tensor. The computation of $\mathcal{G}_{0..500}^{\mathrm{SH},\psi<180^\circ}(\mathrm{LDEM128\_SH}_{0..500})$ is discussed in Text S2.2.1 and the $\mathcal{G}_{0..10800}^{\mathrm{SH},\psi\geq10^\circ}(\mathrm{LDEM128\_SH}_{0..5400})$ term is discussed in Text S2.2.2.

Text S2.2.1. The evaluation of $\mathcal{G}_{0..500}^{\mathrm{SH},\psi<180^\circ}(\mathrm{LDEM128\_SH}_{0..500})$

The term $\mathcal{G}_{0..500}^{\mathrm{SH},\psi<180^\circ}(\mathrm{LDEM128\_SH}_{0..500})$, which we now denote $V_{0..500}^{\mathrm{SH},\psi<180^\circ}(r,\varphi,\lambda)$ in the context of the gravitational potential, was obtained by the equation

$$V_{0..500}^{\mathrm{SH},\psi<180^\circ}(r,\varphi,\lambda)=\frac{\mathrm{GM}}{R}\sum_{n=0}^{500}\left(\frac{R}{r}\right)^{n+1}\sum_{m=-n}^{n}\bar{V}_{nm}^{\mathrm{LDEM128\_SH}_{0..500}}\,\bar{Y}_{nm}(\varphi,\lambda),\qquad(16)$$

where GM is the product of Newton's gravitational constant G (see Text S2.1) and the mass of the Moon $M=7.34630\times10^{22}$ kg (Williams et al., 2014), $R=1727$ km is the radius of the sphere, to which we referenced LDEM128_SH (see Text S1.3) and $\bar{V}_{nm}^{\mathrm{LDEM128\_SH}_{0..500}}$ are the spherical-harmonic coefficients of the gravitational potential

implied by the LDEM128_SH$_{0..500}$ topography. Following Bucha (2025), these coefficients are given as

$$\bar{V}_{nm}^{\text{LDEM128\_SH}_{0..500}} = \frac{2\pi\, R^3}{M} \sum_{p=1}^{P} \sum_{i=0}^{I} S_{npi}\, \overline{\mathrm{H}\rho}_{nm}^{(pi)}, \tag{17}$$

where

$$S_{npi} = \frac{2}{2n+1}\, \frac{1}{n+i+3} \binom{n+i+3}{p} \tag{18}$$

and

$$\overline{\mathrm{H}\rho}_{nm}^{(pi)} = \frac{1}{4\pi} \int_{\varphi'=-\frac{\pi}{2}}^{\frac{\pi}{2}} \int_{\lambda'=0}^{2\pi} \mathrm{H}\rho^{(pi)}(\varphi', \lambda')\, \bar{Y}_{nm}(\varphi', \lambda')\, \mathrm{d}\lambda'\, \cos\varphi'\, \mathrm{d}\varphi' \tag{19}$$

are the spherical-harmonic coefficients of the topographic height-density function

$$\mathrm{H}\rho^{(pi)}(\varphi', \lambda') = \left(\frac{H^{\text{LDEM128\_SH}_{0..500}}(\varphi', \lambda')}{R} \right)^p \rho_i(\varphi', \lambda')\, R^i. \tag{20}$$

The symbol P is the maximum topography power (see p Equation 20) and I is the order of the radial polynomial density coefficients (see Equation 11). To evaluate Equation (17), we used $P = 50$ and $I = 1$. While in theory P approaches infinity (see Bucha, 2025), we have checked that $P = 50$ is sufficient to suppress the truncation error at negligible level for our LDEM128_SH$_{0..500}$ topography (see also Hirt & Kuhn, 2017; Bucha & Kuhn, 2020). The value $I = 1$ is determined by the order of the radial polynomial density coefficients in Equation (15). Equation (16) was evaluated at the lunar surface and on the circumscribing sphere of the radius 1749 km (see Text S1.1) in the same way as Equation (4). Equation (17) was calculated using CHarm.

Text S2.2.2. The evaluation of $\mathcal{G}^{\mathrm{SH},\psi\geq 10^\circ}_{0..10800}(\mathrm{LDEM128\_SH}_{0..5400})$

The computation of $\mathcal{G}^{\mathrm{SH},\psi\geq 10^\circ}_{0..10800}(\mathrm{LDEM128\_SH}_{0..5400})$ from Equation (7), which we shall now denote $V^{\mathrm{SH},\psi\geq 10^\circ}_{0..10800}(r,\varphi,\lambda)$, was slightly different for points at the lunar surface and on the circumscribing sphere.

Let us begin with the circumscribing sphere. In this case, the spherical radius of all points is constant, $r = r_C = 1749$ km. The gravitational potential of the far-zone masses ($\psi \geq 10^\circ$) implied by the topography model $\mathrm{LDEM128\_SH}_{0..5400}$ reads (Bucha, 2025)

$$V^{\mathrm{SH},\psi\geq 10^\circ}_{0..10800}(r_C,\varphi,\lambda) = \frac{\mathrm{GM}}{R}\sum_{n=0}^{10800}\sum_{m=-n}^{n}\bar{V}^{\mathrm{LDEM128\_SH}_{0..5400}}_{nm}(r_C,\psi_0,R)\,\bar{Y}_{nm}(\varphi,\lambda), \tag{21}$$

where $\psi_0 = 10^\circ$ and the spherical-harmonic coefficients are given as

$$\bar{V}^{\mathrm{LDEM128\_SH}_{0..5400}}_{nm}(r_C,\psi_0,R) = \frac{2\pi\,R^3}{M}\sum_{p=1}^{P}\sum_{i=0}^{I}Q_{npi}(r_c,\psi_0,R)\,\overline{\mathrm{H}\rho}^{(pi)}_{nm}. \tag{22}$$

Here, $Q_{npi}(r_c,\psi_0,R)$ are Molodensky's truncation coefficients (for definition and numerical evaluation, see Bucha, 2025) and $\overline{\mathrm{H}\rho}^{(pi)}_{nm}$ are given by Equation (19), but this time with $H^{\mathrm{LDEM128\_SH}_{0..5400}}$ instead of $H^{\mathrm{LDEM128\_SH}_{0..500}}$. Since the truncation degrees of the topography and its implied gravitational potential are now higher compared to the previous paragraph (5400 and 10,800 now vs. 500 and 500 previously in Equation 16), we were forced to decrease P from 50 to 10. As will be shown in Text S3.2, $P = 10$ is fairly sufficient though, because now we are dealing with the gravitational potential of far-zone masses only ($\psi \geq 10^\circ$) which is smooth compared to all masses ($\psi < 180^\circ$) in Equation (16). This is explained by the attenuation of the gravitational field with increasing distance from source (for an example in the spectral domain, see Bucha et al., 2019).

Let us now move to the evaluation of $V^{\mathrm{SH},\psi\geq 10^\circ}_{0..10800}$ from Equation (7) at the lunar topography with varying spherical radius r. It would be highly impractical to use Equation (21)

now, because the spherical-harmonic coefficients in this equation depend on the spherical radius of the evaluation point (r_C in Equation 21). This would generally mean a different set of coefficients for each of the 23,040 × 46,080 ≈ 10^9 points. To overcome this, Bucha et al. (2019) followed Balmino et al. (2012) and Hirt (2012) and employed the upward/downward continuation from some auxiliary sphere of the radius R_a to the topography with the varying radius $r_{\text{surf}}(\varphi, \lambda)$. This technique is called the gradient approach. For simplicity, let $V = V_{0..10800}^{\text{SH},\psi\geq 10^\circ}$. The gradient approach then reads

$$V(r_{\text{surf}}, \varphi, \lambda) = \sum_{k=0}^{K} \frac{1}{k!} \left.\frac{\partial^k V}{\partial r^k}\right|_{r=R_a} (r_{\text{surf}} - R_a)^k. \tag{23}$$

The key to efficiency is to evaluate $\partial^k V/\partial r^k\big|_{r=R_a}$ by efficient FFT-based algorithms and then simply substitute these terms into the truncated Taylor series (23). Note that $\partial^k V/\partial r^k$ requires $\partial^k \bar{V}_{nm}^{\text{LDEM128\_SH}_{0..5400}}(r, \psi_0, R)/\partial r^k$ (see Equation 21), hence $\partial^k Q_{npi}(r, \psi_0, R)/\partial r^k$ (see Equation 22), making the evaluation of $V_{0..10800}^{\text{SH},\psi\geq 10^\circ}$ at the lunar surface a non-trivial task. To this end, we used the equations of Bucha (2025), which are valid for any n, p, i and k. To make the truncation errors of the Taylor series negligible, we used $K = 40$. This choice will be justified in a numerical test in Text S3.2. Again, CHarm was employed to evaluate Equations (21) and (22) together with their radial derivatives.

Text S3. Modeling parameters

This section discusses the truncation degree of V^{GRAIL} from Equation (4) (Text S3.1) and the approximation errors of Equation (6) (Text S3.2).

Text S3.1. Truncation degree of V^{GRAIL} from Equation (4)

Neither too low nor too high truncation degree in Equation (4) is a good choice. If truncated too early, the series will not capture valuable gravitational signals observed by GRAIL. If the series is truncated too late, the following points should be considered.

1. The constraints that were used to estimate GRGM1200B will propagate into the gravitational quantities. For the GRGM1200B variant that we used, the constraint is the Kaula rule, which is an empirical power law. This rule, however, seems to be too strong (Šprlák & Han, 2021) and thus it may smooth GRAIL observations, leaving un-modeled signals in high degrees. Figure 5a of Goossens et al. (2020) shows that the model remains mostly unaffected by the Kaula regularization up to degree 500 (Kaula constraint applied beyond degrees 600). Alternatively, the RM1 variants of GRGM1200B (Goossens et al., 2020) could be used that rely on the gravitational information from topography instead of the Kaula rule. But in principle, this is the same as what our RTM method does, although our RTM does not take advantage of GRAIL observations beyond degree 500 as it happens with GRGM1200B + RM1 models.

2. The series will be subject to the divergence of spherical harmonics at the lunar topography. It has been shown numerically that the potential series evaluated at the lunar surface starts to deviate from the true potential somewhere around degree 700 due to the series divergence (Hirt & Kuhn, 2017; Šprlák & Han, 2021). This is in agreement with the theory, which guarantees convergence outside the smallest lunar circumscribing sphere only (Sansò, 2013). Rigorously speaking, one should therefore reject the idea of evaluating the series at the lunar surface, regardless of the truncation degree. Another

option is to be aware of the divergence and to try to determine the turning point, beyond which partial sums of the series start to deviate from the true value, hoping the bottom part of the series can realistically model the true signal. Such an analysis has been done by Hirt and Kuhn (2017) and Šprlák and Han (2021) and the turning point seems to be somewhere around degree 700.

3. Noise in GRAIL data will be amplified when downward continued to the lunar surface (see Text S5.2) and may even overwhelm the signal.

Considering these points, we decided to truncate the Kaula-constrained GRGM1200B at degree 500.

Text S3.2. Approximation errors of Equation (6)

This section shows that the approximation errors due to Equation (6) are negligible. Since Equation (6) involves the evaluation of Equations (21) and (23) at the lunar topography, this validation will also provide a numerical evidence (not a proof though) that Equation (21) can be used reliably at the lunar topography for $\psi_0 = 10°$ without any signs of the divergence of spherical harmonics.

We calculated the $\mathcal{G}_{0..\infty}^{T,\psi<180°}(\text{LDEM128}_{0..\infty})$ term on the left-hand side of Equation (6) by the tesseroid-based gravity-forward modeling method (Text S2.1) using all topographic masses (global integration). These data will serve as a reference for the test. Given that this is too time consuming, the forward-modeling was conducted only at 360×719 points of all $23{,}040 \times 46{,}080$ LGM2026 points ($0.5° \times 0.5°$ resolution). Importantly, the input topography and density grids were the same as when evaluating LGM2026 maps, that is, they were sampled at the 128-PPD resolution. The right-hand side of Equation (6)

(after the $\approx$ sign) was obtained simply by extracting the data from LGM2026 intermediate results at the corresponding 360×719 grid.

The comparison of both sides of Equation (6) will mostly reflect approximations in $\mathcal{G}^{\mathrm{SH},\psi\geq 10^\circ}_{0..10800}(\mathrm{LDEM128\_SH}_{0..5400})$ due to (a) the truncation of the gravitational field quantities to spherical-harmonic degree 10,800, (b) replacing far-zone masses $\mathrm{LDEM128}_{0..\infty}$ by $\mathrm{LDEM128\_SH}_{0..5400}$, and (c) truncating the originally infinite series over p and k in Equations (22) and (23) at $P = 10$ and $K = 40$, respectively.

Table S1 reports outcomes of the validation at the lunar topography. Discrepancies at the same levels were found also for evaluation points located on the circumscribing sphere while the signals were weaker by 1 order of magnitude at most. Overall, the discrepancies are negligible compared to the overall error budget of LGM2026 (see Section 5 of the main paper), justifying our preference for the more efficient spherical-harmonic-based technique.

Considering that the reference values of this test are independent of spherical-harmonic-based techniques, this validation also proved that Equation (21) does not show any signs of the divergence effect at the lunar surface and thus it can be used to develop LGM2026.

Text S4. Low-frequency RTM correction

This section shows that the 2 independent approaches A and B to the low-frequency RTM correction from Text S1.3.2 lead to comparable results.

In the method A, we used Equation (17) to get spherical-harmonic coefficients of both terms on the right-hand side of Equation (8) (after the $\approx$ sign). Subsequently, both sets of coefficients were rescaled from the sphere of the radius $R = 1727$ km (see Equation 17) to the circumscribing sphere of the radius 1749 km (for the rescaling procedure,

see Barthelmes, 2013). The difference spectrum obtained from the 2 sets of coefficients represents the spectrum of the low-frequency RTM correction on the circumscribing sphere.

In the method B, we harmonically analyzed $V^{\text{RTM without LF}}$, $V^{\text{z,RTM without LF}}$ and $V^{\text{zz,RTM without LF}}$ (see Equation 10) at evaluation points placed on the circumscribing sphere. To this end, we used bivariate splines of degree 3 to interpolate the 23,040 × 46,080 LGM2026 grids into the points of the Driscoll–Healy quadrature and subsequently harmonically analyzed the signals up to degree 11,519. To the coefficients obtained from $V^{\text{z,RTM without LF}}$ and $V^{\text{zz,RTM without LF}}$, we applied the well-known relations from the Meissl scheme to get potential coefficients (e.g., Jekeli, 2017). Note that the method B cannot be used with the gravitational grids at the topography, because spherical-harmonic analysis by quadrature methods requires the signal to be given on a sphere to get solid spherical-harmonic coefficients. These solid spherical-harmonic coefficients can then be used to upward/downward continue gravitational quantities as usually. This is not possible with the quadrature methods if data are given at the topography, although it can sometimes be the only solution for practical reasons (see Rexer et al., 2018).

The results from both methods and their differences are shown in Figure S9. The figure reveals some discrepancies between the 2 methods in the spectral band from 0 to ∼60 whereas good agreement is seen for degrees ∼60 – 500. We attribute the discrepancies mostly to Method B, particularly to the discretization of the lunar topographic masses and to the approximate evaluation of the gravitational field of a tesseroid by the Gauss–Legendre quadrature (Text S2.1). Some portion of the disagreement is, however, also

due to the method A, in which we had to replace $\text{LDEM128}_{0..\infty}$ by $\text{LDEM128\_SH}_{0..5400}$ when evaluating Equation (8). Discrepancies are also seen between the 3 variants of the method B. For degrees up to 2, the method A agrees the most with the method B when the latter is combined with V whereas the worst agreement is seen with V^{zz}. This could be explained by the fact that the gravitational potential is more sensitive to low degrees than its first- and second-order radial derivatives. As another feature visible in Figure S9, the difference spectrum between the method B with V and the method A (the thin dashed blue line) shows an arch-like pattern. This could be associated with the method B, in which the density varied laterally as a step function of the resolution $1^\circ \times 1^\circ$ resolution, while in the method A, the density was a smooth continuous function. In other words, while the original density data were the same for both methods, they entered both methods differently which might produce the arch-like pattern in their difference spectrum. Note that the spectra of a mass distributed over a spherical rectangle (here $1^\circ \times 1^\circ$ density pixels) follows the same arch-like pattern (Pollack, 1973). Overall, Figure S9 reveals that the signal power of the low-frequency correction is 1 or more orders of magnitude weaker than the reference signal from GRAIL.

The coefficients of the low-frequency correction can be used to correct RTM signals. This is possible for the grids residing both at the lunar surface and on the circumscribing sphere. No divergence effect of spherical harmonics (at a detectable level) is expected at the lunar surface, since the low-frequency RTM correction is in our case truncated at degree 500 by definition. From the 2 methods, we opted for the method B in the LGM2026 development. The reason is that it removes the signal that is actually found in our RTM

grids in the spectral band 0 – 500. We used the method B combined with V to correct the RTM signal of the gravitational potential, the method B with V^{z} to correct all 3 elements of the gravitational vector and the method B with V^{zz} to correct all 6 elements of the gravitational tensor. Note that if RTM is applied only at the topography, as frequently done in practice, the grids on the circumscribing sphere are not available. In this case, the method B seems to be a viable alternative method to correct RTM for the low-frequency error.

As an example, Figure S10 shows the low-frequency RTM correction (method B with V^{z}) for V^{z} evaluated at the lunar surface and on the circumscribing sphere. By removing this signal from our RTM grids $V^{z,\text{RTM without LF}}$, we mitigate an interference of artificial RTM signals with GRAIL observations when computing Equation (3). The $1^\circ \times 1^\circ$ rectangles that are visible in the figure are explained by the original $1^\circ \times 1^\circ$ density grids.

All LGM2026 quantities at the lunar surface and on the circumscribing sphere were corrected for the low-frequency RTM signals.

Text S5. Error assessment

This section explains the methods behind the validation of LGM2026 that are reported in Section 5 of the main paper.

Text S5.1. Validation with respect to GRGM1200B

It is useful to validate LGM20226 with respect to a GRAIL-based model, even though LGM2026 depends on GRAIL through the Kaula-constrained GRGM1200B. Such a validation can (a) reveal interference of V^{RTM} with V^{GRAIL} in Equation (3) in harmonics up

to degree 500, (b) check the transition from GRAIL to RTM between degrees 500 and 501 and (c) it can validate LGM2026 a few tens of degrees beyond degree 500, where LGM2026 relies solely on the forward-modeled gravity but the GRAIL model still incorporates real gravitational observations. The reference GRAIL model used here is the GRGM1200B + RM1, $\lambda = 1$. This variant does not rely on the Kaula regularization, but instead incorporates a constraint based on the gravitational field of the lunar topography. It is therefore generally more accurate in high degrees than the Kaula-constrained GRGM1200B.

To be able to validate LGM2026 with respect to GRGM1200B + RM1, $\lambda = 1$ in the spectral domain, a spectral analysis of the LGM2026 grids is necessary. For the same reasons as with the low-frequency correction method B (Text S4), only the LGM2026 grids residing on the circumscribing sphere are suitable for the harmonic analysis. From the ten gravitational quantities of LGM2026, we have harmonically analyzed V and also V^{z} and V^{zz}, because of their simple spectral relation with respect to the gravitational potential V (the Meissl scheme). The remaining quantities that include horizontal derivatives could be analyzed using specialized harmonic analysis methods (e.g., Martinec & Einšpigel, 2018), but this not followed here. We conducted the spherical-harmonic analysis up to degree 11,519 using the Driscoll–Heally quadrature (Driscoll & Healy, 1994). Since LGM2026 grid points do not coincide with the points of the quadrature (offset by a half of the LGM2026 pixel size in both directions), we have interpolated the LGM2026 grids to the quadrature points using bivariate splines of degree 3. After the harmonic

analysis, the coefficients obtained from V^{z} and V^{zz} were transformed into the coefficients of the gravitational potential using the Meissl scheme.

Figure S11 shows the spectra obtained from the 3 quantities. The coefficients from the gravitational potential V are seen to suffer from noise after degree ∼600, making them unusable in this harmonic range. As the signal content in high degrees amplifies with the order of the radial derivative of the gravitational potential, the range of degrees affected by the noise moves beyond ∼2500 and ∼8500 with V^{z} and V^{zz}, respectively. The final spherical-harmonic coefficients were obtained by (a) averaging the solutions from V, V^{z} and V^{zz} in degrees 0 – 500, (b) averaging V^{z} and V^{zz} in degrees 501 –2250 and (c) taking the coefficients from V^{zz} in degrees 2251 – 11,519. These are the coefficients that are validated with respect to GRAIL in Section 5 of the main paper.

To check for the presence of noise in the LGM2026 grids that reside at the topography, we can simply assume that they are square integrable functions and perform *surface* spherical-harmonic analysis of these grids. Although this procedure does not lead to solid spherical-harmonic coefficients of the gravitational field that could be used in the traditional way, it can reveal the presence of noise. Figure S12 confirms that the surface grids do not contain noise in the studied spectral bandwidth. This could be explained by the fact that the gravitational field is stronger at the lunar surface compared to the circumscribing sphere, hence it is easier to capture with our spatial-domain gravity forward modeling.

Text S5.2. Error propagation of GRGM1200B

This section analyzes errors of LGM2026 that are caused by the errors of the spherical-harmonic model GRGM1200B.

Using the 100 clones of the Kaula-constrained GRGM1200B (Goossens et al., 2020), we propagated the errors of GRGM1200B onto the topography and the circumscribing sphere following Sabaka, Nicholas, Goossens, Lemoine, and Mazarico (2014). The characteristics of the errors are reported in Table S2. At the topography, the errors are typically below 0.02 m^2 s^{-2}, 0.4 mGal and 1.1 E for the gravitational potential, the gravitational vector and the gravitational tensor, respectively. On the circumscribing sphere, the errors are smaller by about 1 to 2 orders of magnitude. As discussed by Goossens et al. (2020), the errors of GRGM1200B are calibrated, but it is difficult to assess whether they properly reflect the true errors.

Even if the scaling factor is unknown or biased, the error propagation can realistically capture relative spatial relations of the errors. The errors of V^z are shown in Figure S13. For the other quantities, the errors follow the same spatial pattern, so are not shown. At the lunar surface, the largest errors are observed over low-elevated areas (e.g., the South Pole-Aitken basin) whereas highlands are associated with the smallest errors. This is explained by the downward continuation errors, which generally increase with the distance between the satellites and the topography. On the circumscribing sphere, dominant are latitudinal stripes, which are related to the constellation of the GRAIL satellites. The errors are largest in the equatorial area and smallest in the polar areas, reflecting the satellite ground tracks.

Text S5.3. LDEM128 errors

This section estimates the contribution of LDEM128 errors to LGM2026. LDEM128 errors propagated into LGM2026 in 2 ways: through spatial-domain gravity-forward modeling $\mathcal{G}_{0..\infty}^{T,\psi<10^\circ}(\text{LDEM128}_{0..\infty})$ in Equation (7) for RTM (Text S5.3.1) and through the radius of evaluation points in Equation (4) in the case of the grids at the lunar surface (Text S5.3.2).

Neumann (2024) does not provide error estimates for LDEM128. However, within the $\pm 60^\circ$ latitudinal range, LDEM128 is derived from SLDEM2015 sampled at 256 PPD (Barker et al., 2016). According to Barker et al. (2016), the vertical accuracy of the 512-PPD version of SLDEM2015 is typically $\sim$3 to 4 m. Considering the downsampling to 128 PPD and Figure 1 of Barker et al. (2016), we shall assume that the accuracy of LDEM128 is 8 m.

Text S5.3.1. LDEM128 errors in RTM

Given that rigorous error propagation for high-resolution gravity-forward modeling in the spatial domain is barely possible, we shall use the Monte Carlo method to estimate the errors of $\mathcal{G}_{0..\infty}^{T,\psi<10^\circ}(\text{LDEM128}_{0..\infty})$ that are due to the LDEM128 errors. We generated 100 artificial topography models by adding random errors from the Gaussian distribution to LDEM128, assuming zero mean and variance of 64 m^2. In the absence of information on the spatial autocorrelation of the LDEM128 errors, we assumed no spatial correlation. The density is assumed errorless for now. All 100 topography models were forward-modeled using the tesseroid-based approach from Text S2.1, keeping the same parameters as during the LGM2026 development. Since the spatial-domain gravity-forward modeling

is the most time consuming part of all LGM2026 computations, it is clearly unrealistic to conduct 100 forward-modeling runs using all LGM2026 points. Therefore, we chose 3 representative study areas (Figure S14). Area 1 (Figure S14a) is located in the lunar highlands near the equator and includes the highest lunar topography features (mean surface density $\sim$2280 kg m^{-3}). Area 2 (Figure S14b) is located in the South Pole–Aitken basin and includes the lunar topography of lowest elevations (mean surface density $\sim$2380 kg m^{-3}). Area 3 (Figure S14c) is located in the flat Oceanus Procellarum mare (mean surface density $\sim$2720 kg m^{-3}). The results of the error analysis are summarized in Tables S3, S4 and S5, respectively. Clearly, the errors depend both on the topography and its density. Generally, the standard deviations stay mostly below 0.2 m^2 s^{-2} for V, 1 mGal for V^{z} and about 200 E for V^{zz}. The standard deviations for the horizontal components of the gravitational vector and tensor are typically 1 to 2 orders of magnitude smaller than that for V^{z} and V^{zz}.

We applied the Monte Carlo method also at points on the circumscribing sphere. For brevity, we do not provide detailed statistics, but overall, the errors dropped by 1 to 2 orders of magnitude for the gravitational potential and for the gravitational vector and 3 to 4 orders of magnitude for the gravitational tensor.

Our estimate of the standard deviation for V^{z} can be checked by a simplistic model of the Bouguer plate. If LDEM128 is radially in error with respect to the true topography by $\Delta h = 8$ m, the Bouguer plate predicts the change in V^{z} to be $2\pi\, G\, \rho\, \Delta h = 0.8$ mGal using the mean density of the 3 study areas $\rho = 2460$kg m^{-3}. This is within reasonable agreement with our estimate of 1 mGal.

In the previous error analysis, we assumed the 3D variable density distribution is errorless. While it is straightforward to model the density noise based on the error analysis of the density grids by Goossens et al. (2020), doing so would significantly skew our error estimates. This can be explained as follows. Clearly, the uncertainty of the linear density model increases with depth. Since our topography model is referenced to an internal sphere of the radius 1727 km (see Text S1.3), the largest topographic height is about 21,150 m. This is therefore the height of the highest tesseroid used in gravity-forward modeling $\mathcal{G}_{0..\infty}^{T,\psi<10^\circ}(\text{LDEM128}_{0..\infty})$. Along such long distance, the density uncertainty can significantly increase with the depth, producing large uncertainties of the gravitational quantities. But this is unrealistic for LGM2026, because due to the RTM technique, forward-modeled are in fact only residual masses, that is, masses between LDEM128 and $\text{LDEM128\_SH}_{0..500}$ (see Text S1.3). Considering these actually used residual masses, the largest tesseroid height is 2658 m while the 90th percentile is only 391 m. Thus, the forward-modeled masses that entered LGM2026 never exceeded the ±2658 m range, so the error analysis must reflect this.

Density errors can be incorporated into our error estimates by considering the linear relation between the density and the gravitational field quantities. Goossens et al. (2020) do not provide error analysis for the density model used in the LGM2026 project, only for its different version (see their Section 5.3). For the other version, they estimated the mean error of the surface density to be 11 kg m^{-3} and the mean error of the surface density gradient to be 0.0023 kg m^{-4}. Assuming these numbers could apply also to our density model, the density uncertainty for our tesseroid heights could be expected to be at the level

of a few tens of kg m^{-3}. Compared to the mean density of the lunar crust 2550 kg m^{-3} (Wieczorek et al., 2013), the density errors are only at the level of a few percents of the density itself. Thus, our error estimates from Tables S3, S4 and S5 should be enlarged by a few percents. But given that the data in these tables are estimates themselves, it seems safe to neglect such a small contribution in our error analysis.

Text S5.3.2. LDEM128 errors in Equation (4)

LDEM128 defines the vertical position of the grid, at which LGM2026 provides the lunar surface gravitational field (more precisely, the points reside 0.1 m above LDEM128, see Text S1.1). The vertical uncertainty of LDEM128 thus propagates into the gravitational quantities when synthesizing GRGM1200B. After linearization, the error propagation can be conducted using vertical gradients of the gravitational quantities. Here, we shall use the mean gradients at the lunar surface for simplicity.

Considering the mean value of V^{z} from LGM2026 is roughly -162500 mGal at the lunar surface, an error in the spherical radius of 8 m (see Text S5.3) propagates into an error of 13 m^2 s^{-2} in V. With the mean value of $V^{zz} = 1830$ E from the LGM2026 surface maps, an error of 1.5 mGal in V^{z} can be expected at the distance of 8 m. Given that V^{xz} and V^{yz} are about 1 order of magnitude smaller than V^{zz} (cf. Figures S4b, S4c and S3c), the errors of V^{x} and V^{y} will also be an order of magnitude smaller compared to the errors of V^{z}. The error estimation for the gravitational tensor is difficult, because LGM2026 does not show the third-order gravitational gradients. But the approximate relation $V^{zzz} \approx -6\,\frac{G\,M}{(1{,}737{,}400\ \mathrm{m})^4} = -3.2\ \times 10^{-12}\ \mathrm{m^{-1}\ s^{-2}}$ (see Text S2 for the values of G and M) leads to an error of 0.025 E for V^{zz}. Since the gravitational field of planetary

objects typically varies more in the radial direction than in the horizontal directions (see, for instance, the magnitudes at the scales of Figure S2), the error estimates for the remaining elements of the gravitational tensor will not exceed the 0.025 E error for V^{zz}.

Relative to the other error sources, the error of the vertical position of the evaluation point grid is by far the most significant for the gravitational potential and is safely negligible for the gravitational tensor. For the gravitational vector, it is comparable to the other sources of errors. Importantly, these error estimates are tied to the gravitational quantities of LGM2026. Once the concept of the disturbing field is introduced (e.g., Hofmann-Wellenhof & Moritz, 2005), so that one works with quantities such as the disturbing potential, gravity anomalies or deflections of the vertical, then the errors due to the vertical position of evaluation points fall a few orders of magnitude (e.g., 3 or 4 orders for the disturbing potential) and thus become safely negligible compared to other error sources. This is explained by the fact that the magnitudes of the vertical gradients of disturbing field quantities are smaller by a few orders compared to the gradients of gravitational quantities. For instance, the magnitude of the radial derivative of the disturbing potential (gravity disturbance in spherical approximation) at the lunar surface is typically at the order of $\sim 10^2$ mGal, while the magnitude of the radial derivative of the gravitational potential is $\sim 1.6 \times 10^5$ mGal (see Figure S2c).

Text S5.4. Errors of spatial-domain gravity-forward modeling

This section estimates the internal accuracy of the spatial-domain gravity-forward modeling $\mathcal{G}_{0..\infty}^{T,\psi<10^\circ}(\mathrm{LDEM128}_{0..\infty})$. This validation is necessary, because the method requires

some empirical choices, most notably to choose the orders of the Gauss–Legendre quadrature (see Text S2.1).

In this internal validation, we compared the gravitational effects $\mathcal{G}_{0..\infty}^{T,\psi<10^\circ}(\mathrm{LDEM128}_{0..\infty})$ from LGM2026 with respect to 2 solutions relying on higher orders of the Gauss–Legendre quadrature (see Text S2.1). We chose 2 higher-order solutions to illustrate that further increasing the quadrature orders would likely lead to marginal improvements only. For the same reasons as in Text S5.3.1, the numerical experiment is conducted over the 3 study areas from Figure S14. The results of the test are reported in Tables S6, S7 and S8. Generally, the errors are the largest over the rugged area 1, which features the highest peaks of the lunar topography. Over the flat topography of medium heights in area 3, the errors are the smallest. Somewhere in between are the errors over the area 2, which is rugged but its elevations are the smallest of the entire lunar surface.

Overall, we conclude that the accuracy is typically at the order 10^{-3} $\mathrm{m^2\ s^{-2}}$ or better for the gravitational potential, 1 mGal or better for the gravitational vector and 100 E or better for the gravitational tensor. Compared to the error sources from Texts S5.2, S5.3.1 and S5.3.2, the errors of the gravitational potential are safely negligible, while the errors of gravitational vector and tensor are roughly at the same level as the other error sources.

We repeated the experiment also on the circumscribing sphere, but do not provide detailed statistics for the sake of brevity. Compared to the already reported errors at the lunar topography, the errors of the gravitational potential remained at the same order of magnitude, the errors of the gravitational vector dropped by 1 to 3 orders of magnitude and the errors of the gravitational tensor dropped by 3 to 5 orders of magnitude. Thus

for the LGM2026 maps on the circumscribing sphere, these errors reach for all quantities similar magnitudes compared to the other error sources.

Text S5.5. Errors of spectral-domain gravity-forward modeling

We consider the internal errors of spectral-domain gravity forward modeling in $\mathcal{G}_{0..500}^{\mathrm{SH},\psi<180^\circ}(\mathrm{LDEM128\_SH}_{0..500})$ (see Equation 7) negligible compared to other error sources. The reason is that it is well-known from the literature (e.g., Hirt & Kuhn, 2014; Hirt et al., 2016; Hirt & Kuhn, 2017; Rexer, 2017; Hirt, Yang, et al., 2019; Bucha & Sansò, 2021; Bucha, 2025) that it evaluates gravitational field quantities accurately as long as a sufficiently large number of topography powers is employed (here 50 powers, see Text S2.2) and if the spectral content of the topography powers $p > 1$ found beyond the resolution of the input topography is properly taken into account as done in our computations. In that case, it can evaluate, for instance, the gravitational vector with a global root mean square error at the order of a few μGal or even less (see the references above).

Based on our error analysis from Section S3.2, we also neglected the internal errors of $\mathcal{G}_{0..10800}^{\mathrm{SH},\psi\geq10^\circ}(\mathrm{LDEM128\_SH}_{0..5400})$ (see Equation 7).

Text S5.6. Comparison with respect to LGM2011

Figure S15 compares LGM2026 with respect to LGM2011 using global maps of the gravitational acceleration. Discussion to the figure is provided in Section 5 of the main paper. Here, we would like to point out the limitations of this comparison. The LGM2026 maps are expressed in the Moon's principal axes coordinate system. On the other hand, the topography-implied gravity from LGM2011 relies on a topography model from the

LRO mission, which is given in the Mean-Earth/Polar-Axis coordinate system. The difference between these coordinate systems can reach 875 m (Neumann, 2024). To be able to perform a simple pixel-to-pixel comparison, we neglected the fact that both models are expressed in different coordinate systems. Given the 1.5-km resolution of LGM2011 at the equator, this seems to be permissible within reasonable error limits. Another option would be to transform LGM2011 pixel-by-pixel to the Moon's principle axes coordinate system, leading to irregularly distributed pixels, and then to interpolate into a regular grid. In this way, the coordinate systems would match, but this approach produces another kind of errors, namely the interpolation errors.

Finally, Figure S16 visualizes LGM2026 and LGM2011 in their full resolution over a small region in the South Pole–Aitken basin. Thanks to its ∼6-times higher resolution, LGM2026 reveals gravitational field features that are invisible to LGM2011.

Text S5.7. Artifacts in LDEM128

LDEM128 is a state-of-the-art model of the lunar topography. This does not mean, however, that it is free of artifacts or errors. Artifacts in LDEM128 propagated into LGM2026 in at least 2 ways. First, they affected the V^{GRAIL} term in Equation (4) through the radial coordinate of evaluation points. Second, they affected spatial-domain gravity-forward modeling when evaluating $\mathcal{G}_{0..\infty}^{T,\psi<10^\circ}(\mathrm{LDEM128}_{0..\infty})$ in Equation (7). An example of LGM2026 artifacts caused by LDEM128 is shown in Figure S17. Removal of the artifacts from LDEM128 prior to gravity field modeling—as done, for instance, in SRTM2gravity (Hirt, Yang, et al., 2019)—would certainly be desirable, but this is not a straightforward task due to the nature of the artifacts. A decision has therefore been

made to use LDEM128 as is. Least affected by the artifacts is the gravitational potential while the gravitational tensor is affected the most (relative to the signal strength).

References

Balmino, G., Vales, N., Bonvalot, S., & Briais, A. (2012). Spherical harmonic modelling to ultra-high degree of Bouguer and isostatic anomalies. *Journal of Geodesy*, *86*, 499–520. doi: 10.1007/s00190-011-0533-4

Barker, M. K., Mazarico, E., Neumann, G. A., Zuber, M. T., Haruyama, J., & Smith, D. E. (2016). A new lunar digital elevation model from the Lunar Orbiter Laser Altimeter and SELENE Terrain Camera. *Icarus*, *273*, 346–355. doi: 10.1016/j.icarus.2015.07.039

Barthelmes, F. (2013). *Definition of functionals of the geopotential and their calculation from spherical harmonic models: Theory and formulas used by the calculation service of the International Centre for Global Earth models (ICGEM),* `http://icgem.gfz-potsdam.de` (Scientific Technical Report No. STR09/02). Potsdam, Germany: GFZ German Research Centre for Geosciences. doi: 10.2312/GFZ.b103-0902-26

Bucha, B. (2022). Spherical harmonic synthesis of area-mean potential values on irregular surfaces. *Journal of Geodesy*, *96*(68). doi: 10.1007/s00190-022-01658-1

Bucha, B. (2025). Spectral gravity forward modelling of 3D variable densities using an arbitrary integration radius with application to lunar topographic masses. *Journal of Geodesy*, *99*(31). doi: 10.1007/s00190-025-01951-9

Bucha, B., Hirt, C., & Kuhn, M. (2019). Cap integration in spectral gravity forward

modelling: near- and far-zone gravity effects via Molodensky's truncation coefficients. *Journal of Geodesy*, *93*, 65–83. doi: 10.1007/s00190-018-1139-x

Bucha, B., & Kuhn, M. (2020). A numerical study on the integration radius separating convergent and divergent spherical harmonic series of topography-implied gravity. *Journal of Geodesy*, *94*, 112. doi: 10.1007/s00190-020-01442-z

Bucha, B., & Sansò, F. (2021). Gravitational field modelling near irregularly shaped bodies using spherical harmonics: a case study for the asteroid (101955) Bennu. *Journal of Geodesy*, *95*, 56. doi: 10.1007/s00190-021-01493-w

Chin, G., Brylow, S., Foote, M., Garvin, J., Kasper, J., Keller, J., ... Zuber, M. (2007). Lunar Reconnaissance Orbiter overview: the instrument suite and mission. *Space Science Reviews*, *129*, 391–419. doi: 10.1007/s11214-007-9153-y

Driscoll, J. R., & Healy, D. M. (1994). Computing Fourier transforms and convolutions on the 2-sphere. *Advances in Applied Mathematics*, *15*, 202–250.

Ďuríčková, Z., & Janák, J. (2016). RTM-based omission error corrections for global geopotential models: case study in Central Europe. *Studia Geophysica et Geodaetica*, *60*, 622–643. doi: 10.1007/s11200-015-0598-2

Forsberg, R., & Tscherning, C. C. (1981). The use of height data in gravity field approximation by collocation. *Journal of Geophysical Research*, *86*, 7843–7854. doi: 10.1029/JB086iB09p07843

Goossens, S., Sabaka, T. J., Wieczorek, M. A., Neumann, G. A., Mazarico, E., Lemoine, F. G., ... Zuber, M. T. (2020). High-resolution gravity field models from GRAIL data and implications for models of the density structure of the Moon's crust. *Journal of*

Geophysical Research: Planets, *125*, e2019JE006086. doi: 10.1029/2019JE006086

Grombein, T., Seitz, K., & Heck, B. (2017). On high-frequency topography-implied gravity signals for a height system unification using GOCE-based global geopotential models. *Surveys in Geophysics*, *38*, 443–477. doi: 10.1007/s10712-016-9400-4

Hirt, C. (2012). Efficient and accurate high-degree spherical harmonic synthesis of gravity field functionals at the Earth's surface using the gradient approach. *Journal of Geodesy*, *86*, 729–744. doi: 10.1007/s00190-012-0550-y

Hirt, C., Bucha, B., Yang, M., & Kuhn, M. (2019). A numerical study of residual terrain modelling (RTM) techniques and the harmonic correction using ultra-high-degree spectral gravity modelling. *Journal of Geodesy*, *93*, 1469–1486. doi: 10.1007/s00190-019-01261-x

Hirt, C., Claessens, S., Fecher, T., Kuhn, M., Pail, R., & Rexer, M. (2013). New ultrahigh-resolution picture of Earth's gravity field. *Geophysical Research Letters*, *40*, 4279–4283. doi: 10.1002/grl.50838

Hirt, C., & Kuhn, M. (2014). Band-limited topographic mass distribution generates full-spectrum gravity field: Gravity forward modeling in the spectral and spatial domains revisited. *Journal of Geophysical Research: Solid Earth*, *119*, 3646–3661. doi: 10.1002/2013JB010900

Hirt, C., & Kuhn, M. (2017). Convergence and divergence in spherical harmonic series of the gravitational field generated by high-resolution planetary topography—A case study for the Moon. *Journal of Geophysical Research: Planets*, *122*, 1727–1746. doi: 10.1002/2017JE005298

Hirt, C., Kuhn, M., Claessens, S., Pail, R., Seitz, K., & Gruber, T. (2014). Study of the Earth's short-scale gravity field using the ERTM2160 gravity model. *Computers and Geosciences*, *73*, 71–80. doi: 10.1016/j.cageo.2014.09.001

Hirt, C., Reußner, E., Rexer, M., & Kuhn, M. (2016). Topographic gravity modeling for global Bouguer maps to degree 2160: Validation of spectral and spatial domain forward modeling techniques at the 10 microgal level. *Journal of Geophysical Research: Solid Earth*, *121*, 6846–6862. doi: 10.1002/2016JB013249

Hirt, C., Yang, M., Kuhn, M., Bucha, B., Kurzmann, A., & Pail, R. (2019). SRTM2gravity: an ultrahigh resolution global model of gravimetric terrain corrections. *Geophysical Research Letters*, *46*, 4618–4627. doi: 10.1029/2019GL082521

Hofmann-Wellenhof, B., & Moritz, H. (2005). *Physical Geodesy*. Wien, New York: Springer.

Hu, X., & Jekeli, C. (2015). A numerical comparison of spherical, spheroidal and ellipsoidal harmonic gravitational field models for small non-spherical bodies: examples for the Martian moons. *Journal of Geodesy*, *89*, 159–177. doi: 10.1007/s00190-014-0769-x

Jekeli, C. (2017). *Spectral methods in geodesy and geophysics*. CRC Press.

Kato, M., Sasaki, S., Takizawa, Y., & the Kaguya project team. (2010). The Kaguya mission overview. *Space Science Reviews*, *154*, 3–19. doi: 10.1007/s11214-010-9678-3

Lin, M., Denker, H., & Müller, J. (2020). Gravity field modeling using tesseroids with variable density in the vertical direction. *Surveys in Geophysics*, *41*, 723–765. doi:

10.1007/s10712-020-09585-6

Martinec, Z., & Einšpigel, D. (2018). SHAVEL: A program for the spherical harmonic analysis of a horizontal vector field sampled in an equiangular grid on a sphere. *Computer Physics Communications*, *233*, 206–214. doi: 10.1016/j.cpc.2018.06.015

Neumann, G. A. (2024). *LOLA MOON_PA gridded dataset [Data set]. NASA Goddard Space Flight Center Planetary Geodesy Data Archive.* doi: 10.60903/LOLA_PA

Pollack, H. N. (1973). Spherical harmonic representation of the gravitational potential of a point mass, a spherical cap and a spherical rectangle. *Journal of Geophysical Research*, *78*, 1760-1768. doi: 10.1029/JB078i011p01760

Rexer, M. (2017). *Spectral solutions to the topographic potential in the context of high-resolution global gravity field modelling* (Unpublished doctoral dissertation). Technische Universität München, München, Germany.

Rexer, M., Hirt, C., Bucha, B., & Holmes, S. (2018). Solution to the spectral filter problem of residual terrain modelling (RTM). *Journal of Geodesy*, *92*, 675–690. doi: 10.1007/s00190-017-1086-y

Sabaka, T. J., Nicholas, J. B., Goossens, S., Lemoine, F. G., & Mazarico, E. (2014). *Error propagation for high-degree gravity models developed from the GRAIL mission.* `https://pds-geosciences.wustl.edu/grail/grail-l-lgrs-5-rdr-v1/grail_1001/extras/clones/clone_description.pdf`, (accessed October 02, 2025).

Sansò, F. (2013). Harmonic Calculus and Global Gravity Models. In F. Sansò & M. G. Sideris (Eds.), *Geoid determination: Theory and methods* (pp. 111–168).

Berlin, Heidelberg: Springer-Verlag.

Šprlák, M., & Han, S.-C. (2021). On the use of spherical harmonic series inside the minimum Brillouin sphere: theoretical review and evaluation by GRAIL and LOLA satellite data. *Earth-Science Reviews*, *222*, 103739. doi: 10.1016/j.earscirev.2021.103739

Tiesinga, E., Mohr, P. J., Newell, D. B., & Taylor, B. N. (2021). CODATA recommended values of the fundamental physical constants: 2018. *Reviews of Modern Physics*, *93*. doi: 10.1103/RevModPhys.93.025010

Wieczorek, M. A. (2024). *Spherical harmonic models of the shape of the Moon (principal axis coordinate system) [LDEM128] (1.0.0) [Data set].* doi: 10.5281/zenodo.11533784

Wieczorek, M. A., Neumann, G. A., Nimmo, F., Kiefer, W. S., Taylor, G. J., Melosh, H. J., ... Zuber, M. T. (2013). The crust of the Moon as seen by GRAIL. *Science*, *339*, 671–675. doi: 10.1126/science.1231530

Williams, J. G., Konopliv, A. S., Boggs, D. H., Park, R. S., Yuan, D.-H., Lemoine, F. G., ... Zuber, M. T. (2014). Lunar interior properties from the GRAIL mission. *Journal of Geophysical Research: Planets*, *119*, 1546–1578. doi: 10.1002/2013JE004559

Zuber, M. T., Smith, D. E., Watkins, M. M., Asmar, S. W., Konopliv, A. S., Lemoine, F. G., ... Yuan, D.-N. (2013). Gravity field of the Moon from the Gravity Recovery and Interior Laboratory (GRAIL) mission. *Science*, *339*, 668–671. doi: 10.1126/science.1231507

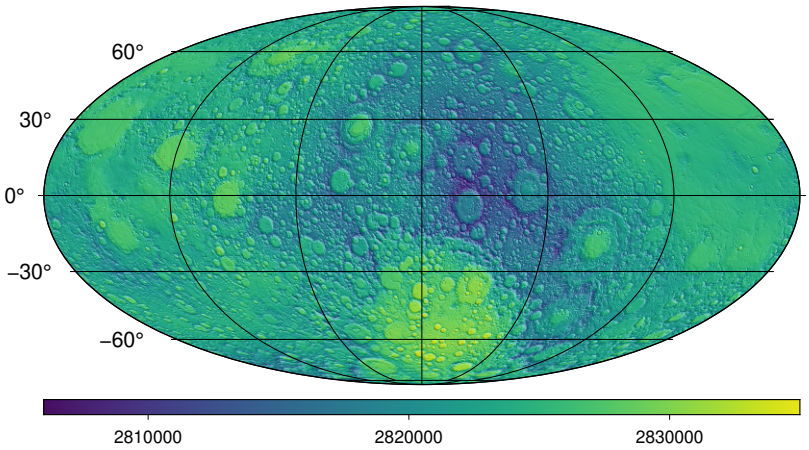

Figure S1. LGM2026 map of the gravitational potential at the lunar surface ($m^2\ s^{-2}$).

The map is downsampled for visualization purposes and is centered at the 180° meridian.

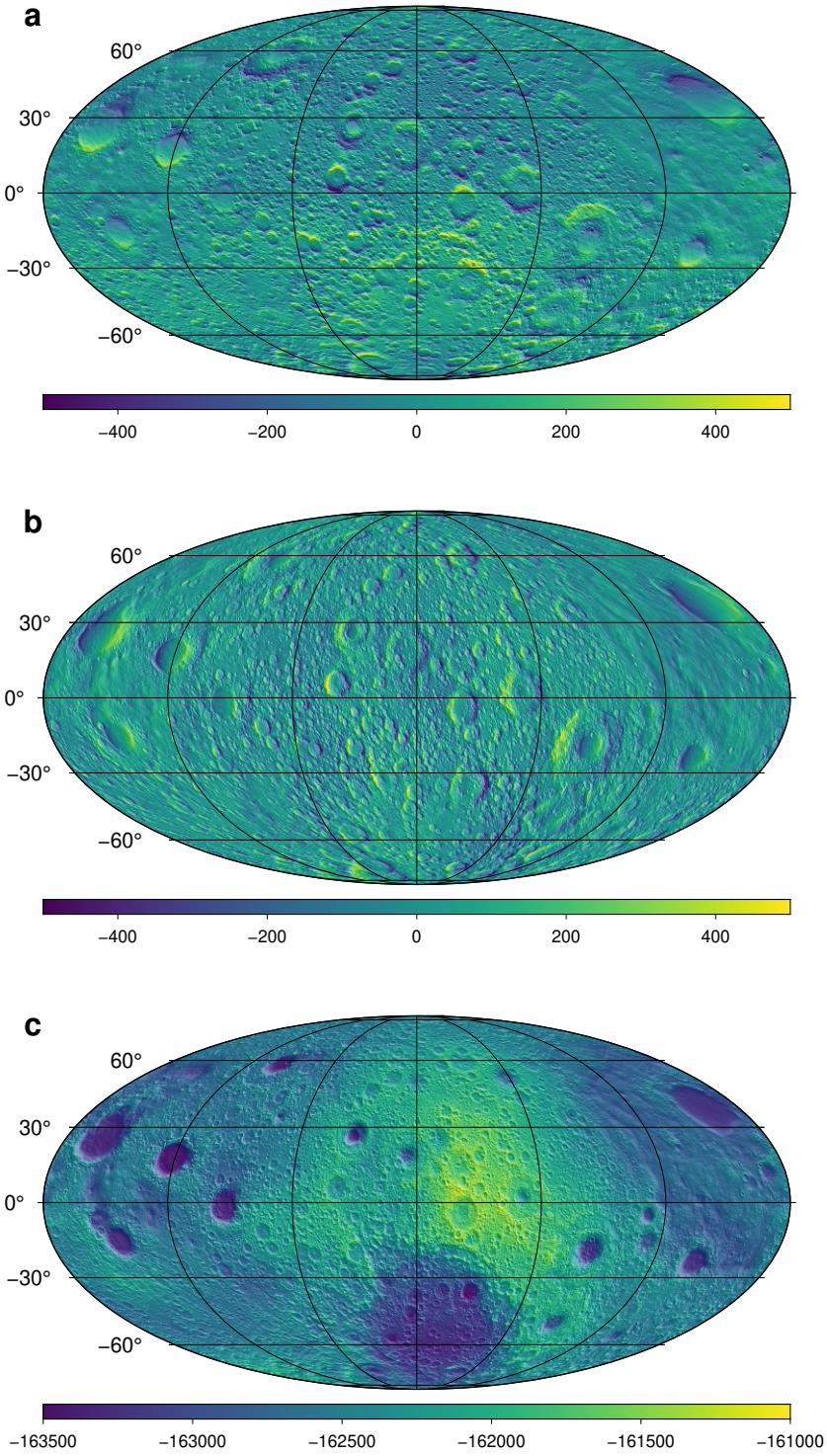

Figure S2. LGM2026 maps of the gravitational vector elements V^{x} (a), V^{y} (b) and V^{z} (c) at the lunar surface (mGal; 1 mGal = 10^{-5} m s^{-2}). The maps are downsampled for visualization purposes and are centered at the 180° meridian.

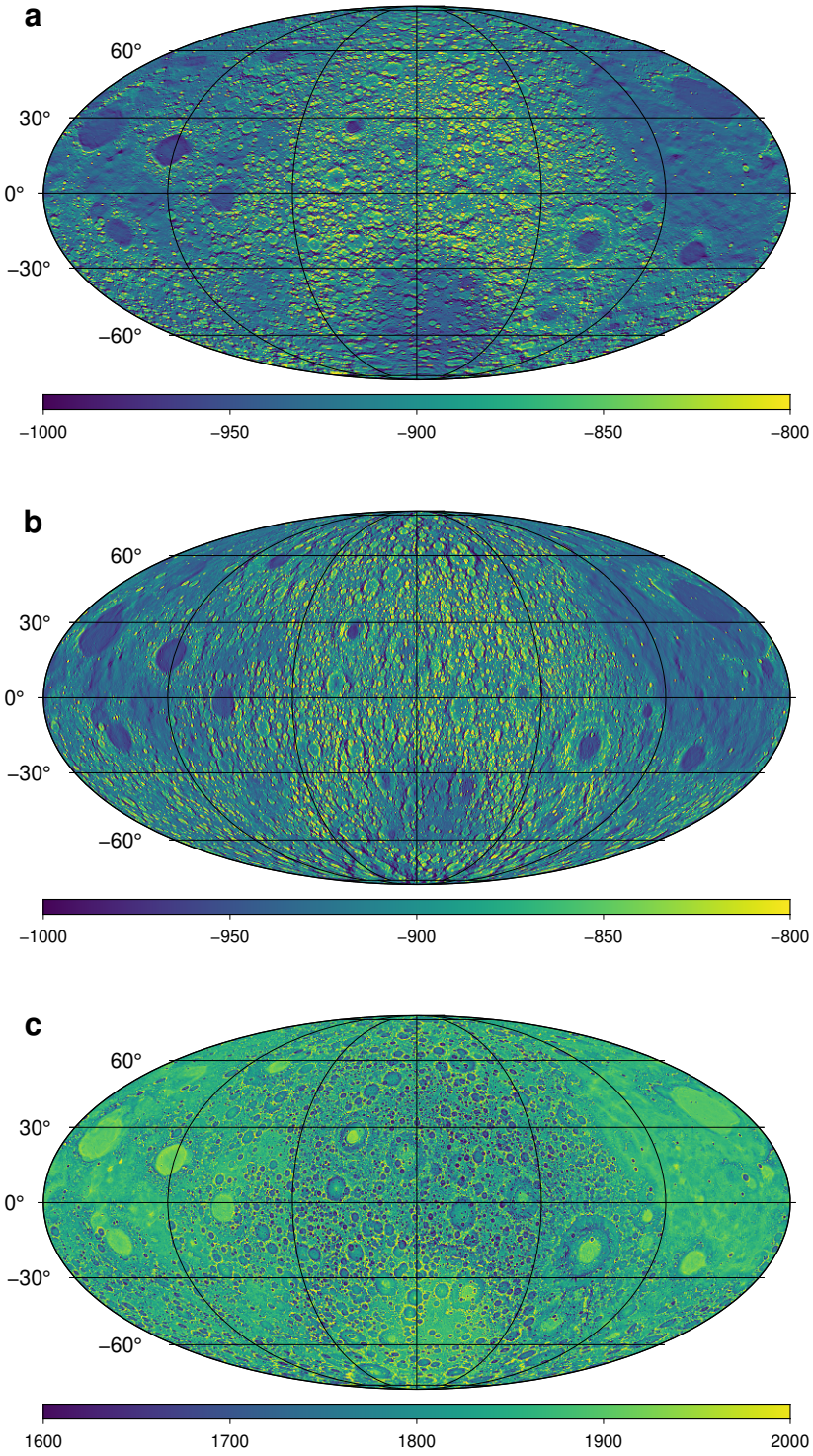

Figure S3. LGM2026 maps of the diagonal elements of the gravitational tensor V^{xx} (a), V^{yy} (b), V^{zz} (c) at the lunar surface (E; 1 E = 10^{-9} s^{-2}). The maps are downsampled for visualization purposes and are centered at the 180° meridian.

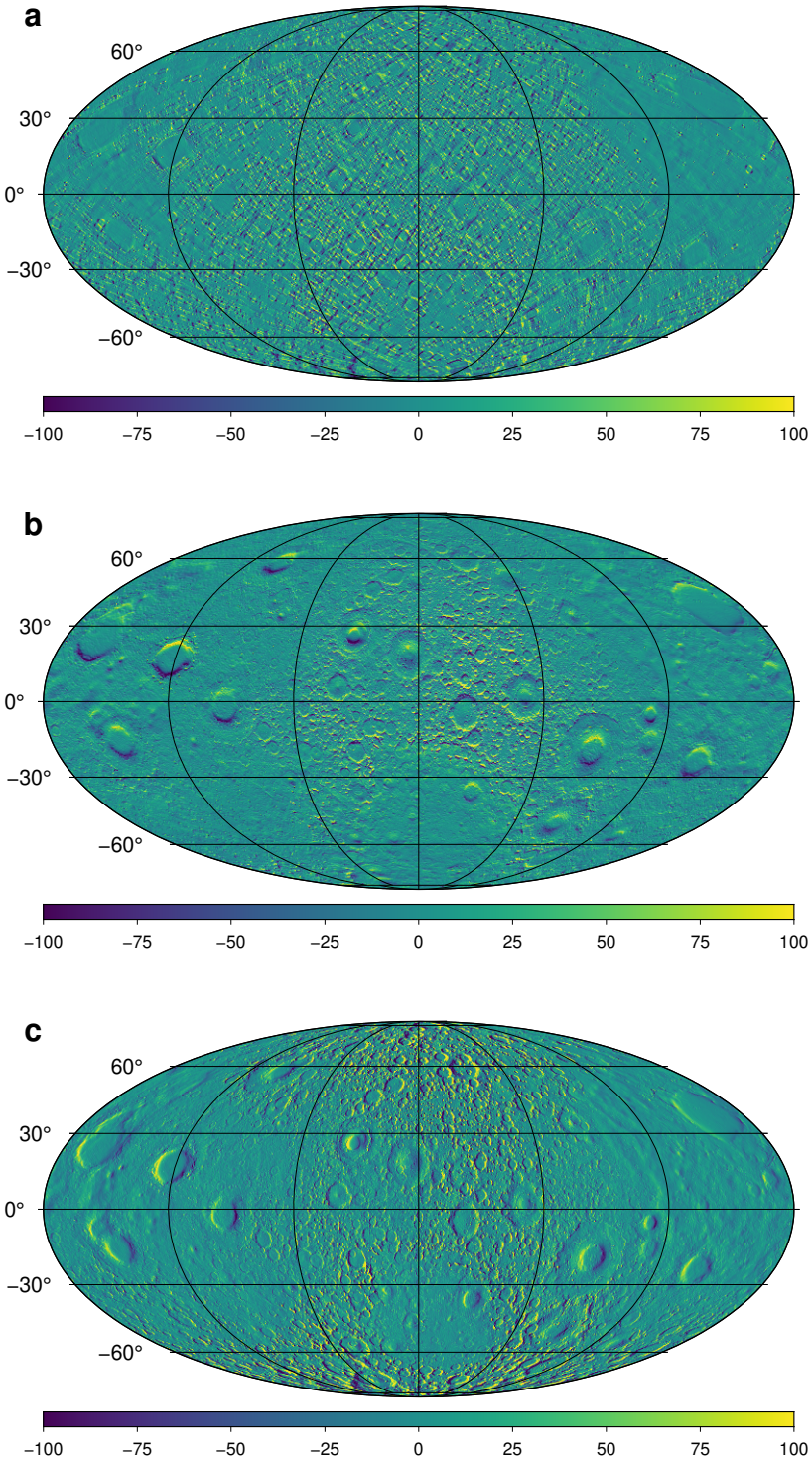

Figure S4. LGM2026 maps of the off-diagonal elements of the gravitational tensor V^{xy} (a), V^{xz} (b) and V^{yz} (c) at the lunar surface (E). The maps are downsampled for visualization purposes and are centered at the 180° meridian.

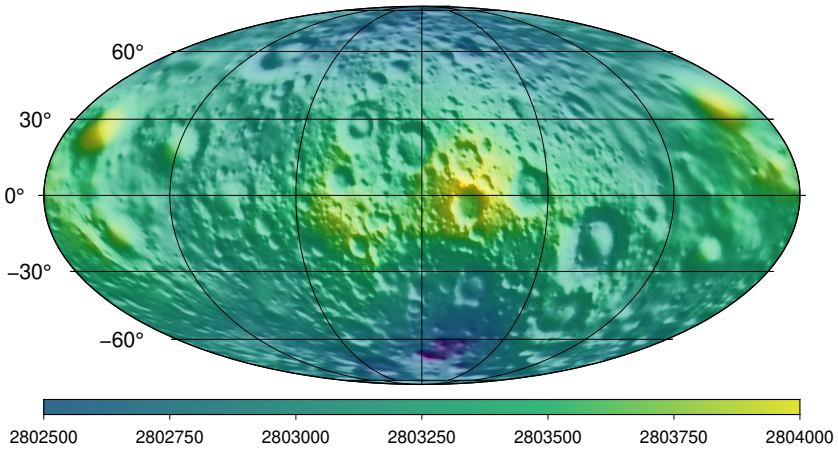

Figure S5. LGM2026 map of the gravitational potential on the circumscribing sphere (m^2 s^{-2}). The map is downsampled for visualization purposes and is centered at the 180° meridian.

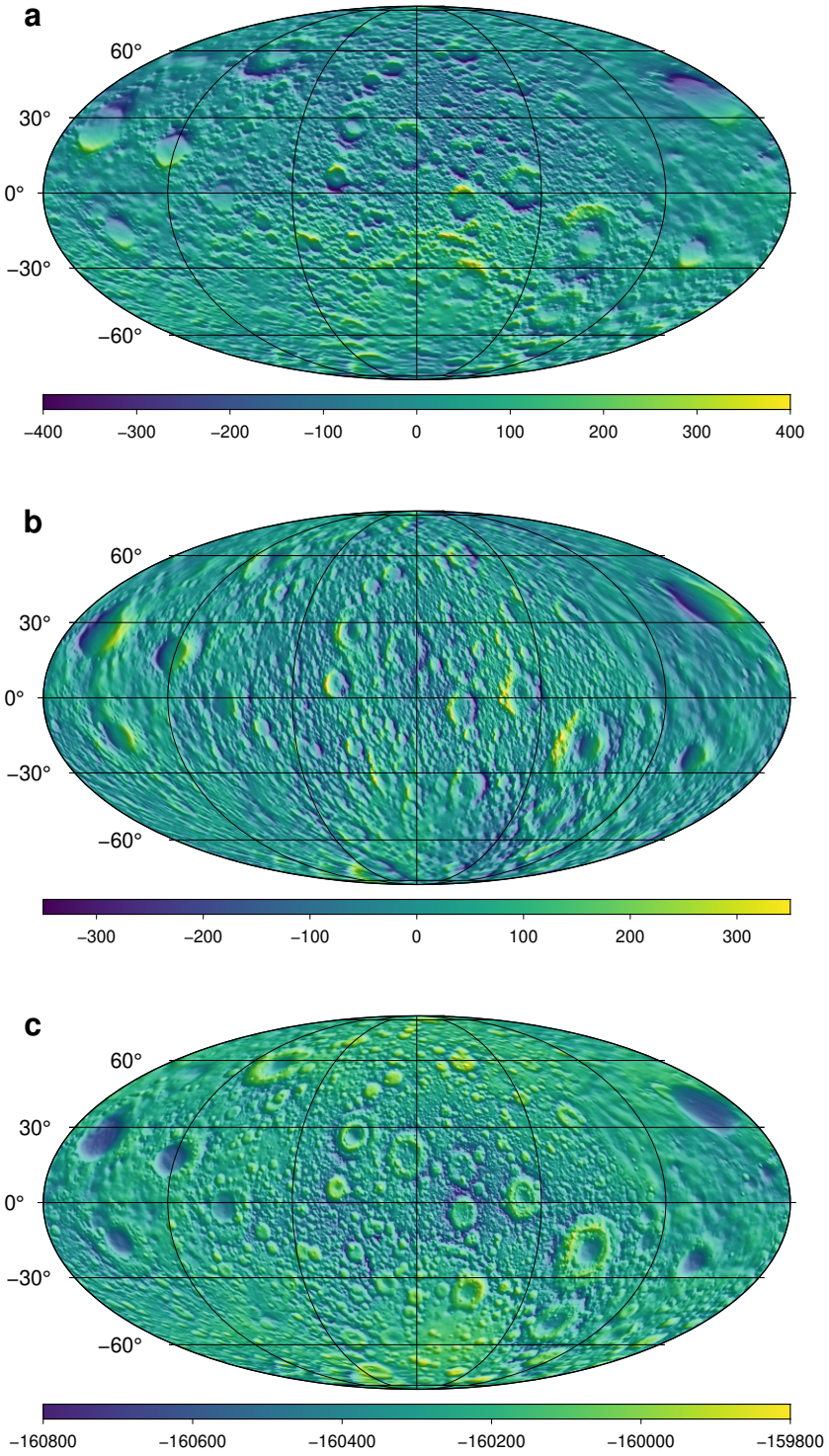

Figure S6. LGM2026 maps of the gravitational vector elements V^{x} (a), V^{y} (b) and V^{z} (c) on the circumscribing sphere (mGal). The maps are downsampled for visualization purposes and are centered at the 180° meridian.

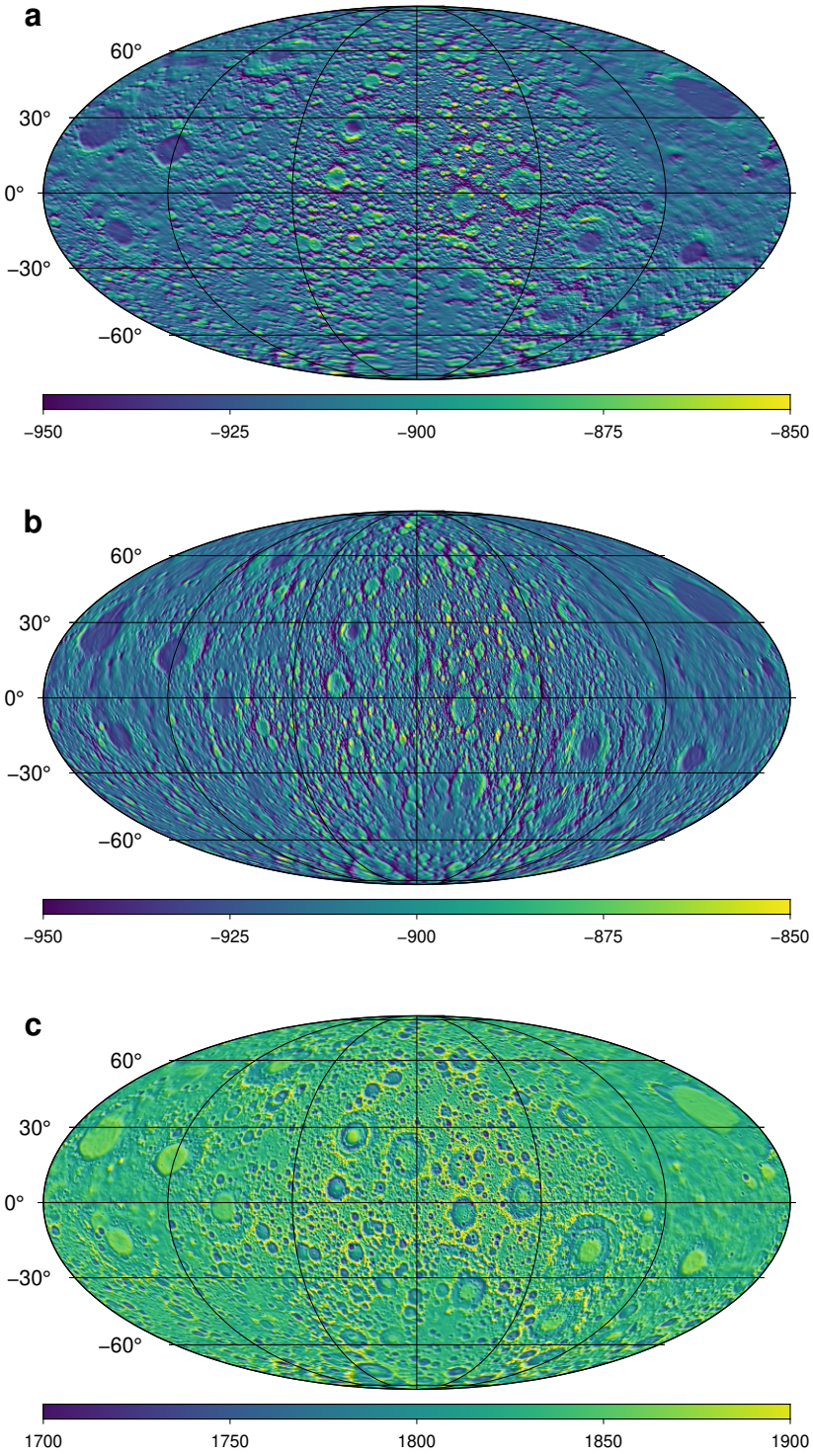

Figure S7. LGM2026 maps of the diagonal elements of the gravitational tensor V^{xx} (a), V^{yy} (b), V^{zz} (c) on the circumscribing sphere (E). The maps are downsampled for visualization purposes and are centered at the 180° meridian.

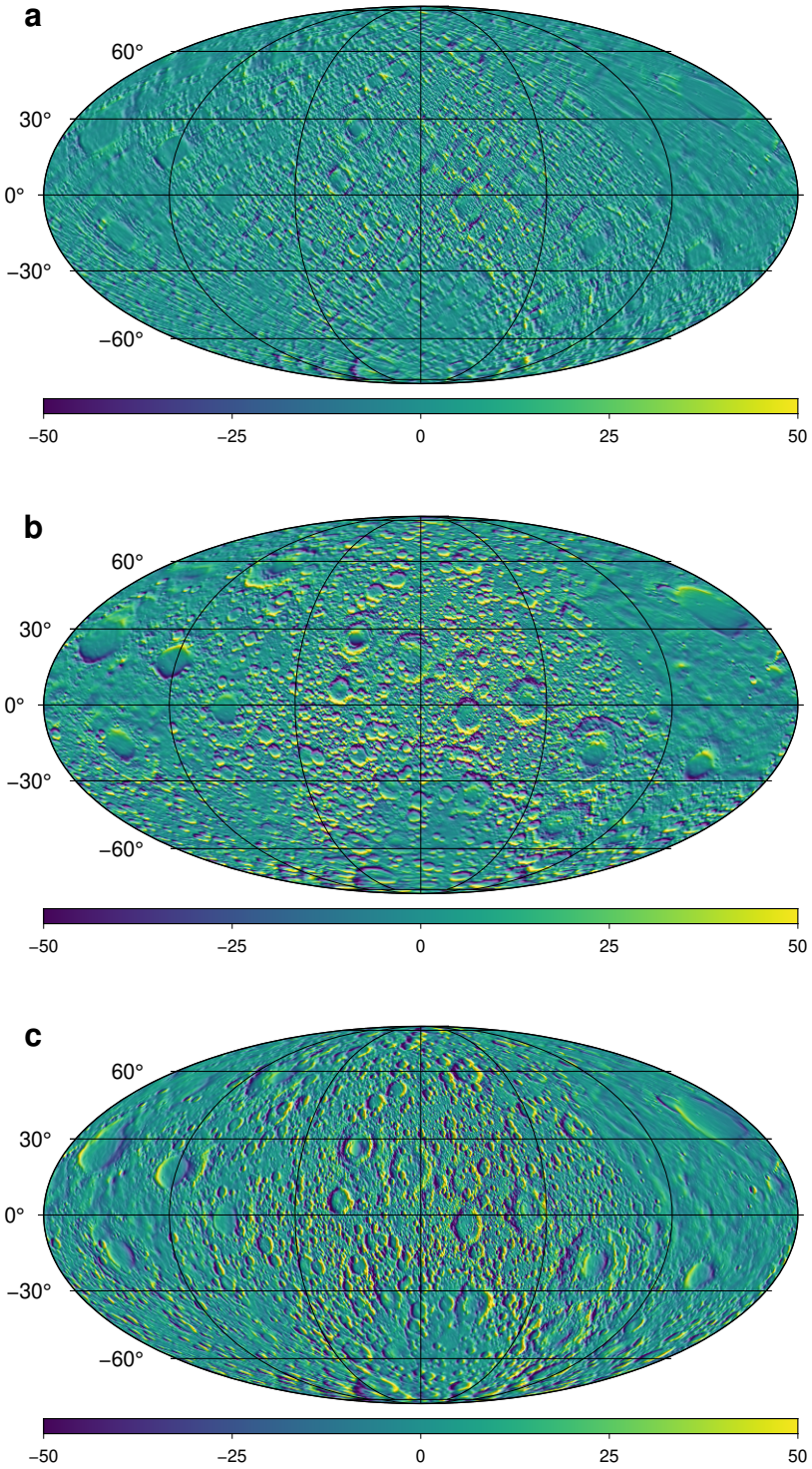

Figure S8. LGM2026 maps of the off-diagonal elements of the gravitational tensor V^{xy} (a), V^{xz} (b) and V^{yz} (c) on the circumscribing sphere (E). The maps are downsampled for visualization purposes and are centered at the 180° meridian.

Table S1. Approximation errors of Equation (6). Shown are statistics of the reference signals from spatial-domain gravity forward modeling (the left-hand side of Equation 6) and statistics of the discrepancies of the new approach (the right-hand side of Equation 6 minus the left-hand side). STD stands for the standard deviation.

	Reference signal				Discrepancies			
Quantity	min	max	mean	STD	min	max	mean	STD
V [m^2 s^{-2}]	3.4e+04	4.1e+04	3.6e+04	1.5e+03	-2.9e-02	1.9e-01	8.3e-02	1.6e-02
V^x [mGal]	-6.8e+02	1.2e+03	3.8e+00	1.7e+02	-2.1e-02	4.0e-02	4.1e-03	4.4e-03
V^y [mGal]	-7.9e+02	7.6e+02	-1.8e-02	1.7e+02	-2.7e-02	3.2e-02	-2.7e-04	5.1e-03
V^z [mGal]	-3.3e+03	-1.1e+03	-2.1e+03	2.6e+02	-5.6e-03	1.3e-03	-2.4e-03	5.2e-04
V^{xx} [E]	-5.1e+02	7.2e+02	-1.1e+00	8.4e+01	-1.0e-03	1.6e-03	1.0e-04	1.8e-04
V^{xy} [E]	-3.2e+02	3.7e+02	-8.1e-02	4.6e+01	-1.4e-03	1.4e-03	-1.7e-06	2.3e-04
V^{xz} [E]	-6.3e+02	6.3e+02	3.8e-01	9.5e+01	-4.1e-04	2.1e-04	-4.2e-05	4.4e-05
V^{yy} [E]	-5.3e+02	6.5e+02	-1.3e+00	8.4e+01	-1.4e-03	1.4e-03	-1.7e-05	2.0e-04
V^{yz} [E]	-6.3e+02	6.7e+02	1.5e-01	9.5e+01	-3.2e-04	2.8e-04	2.8e-06	5.2e-05
V^{zz} [E]	-1.2e+03	8.1e+02	2.4e+00	1.4e+02	-8.9e-04	7.6e-04	-8.4e-05	1.4e-04

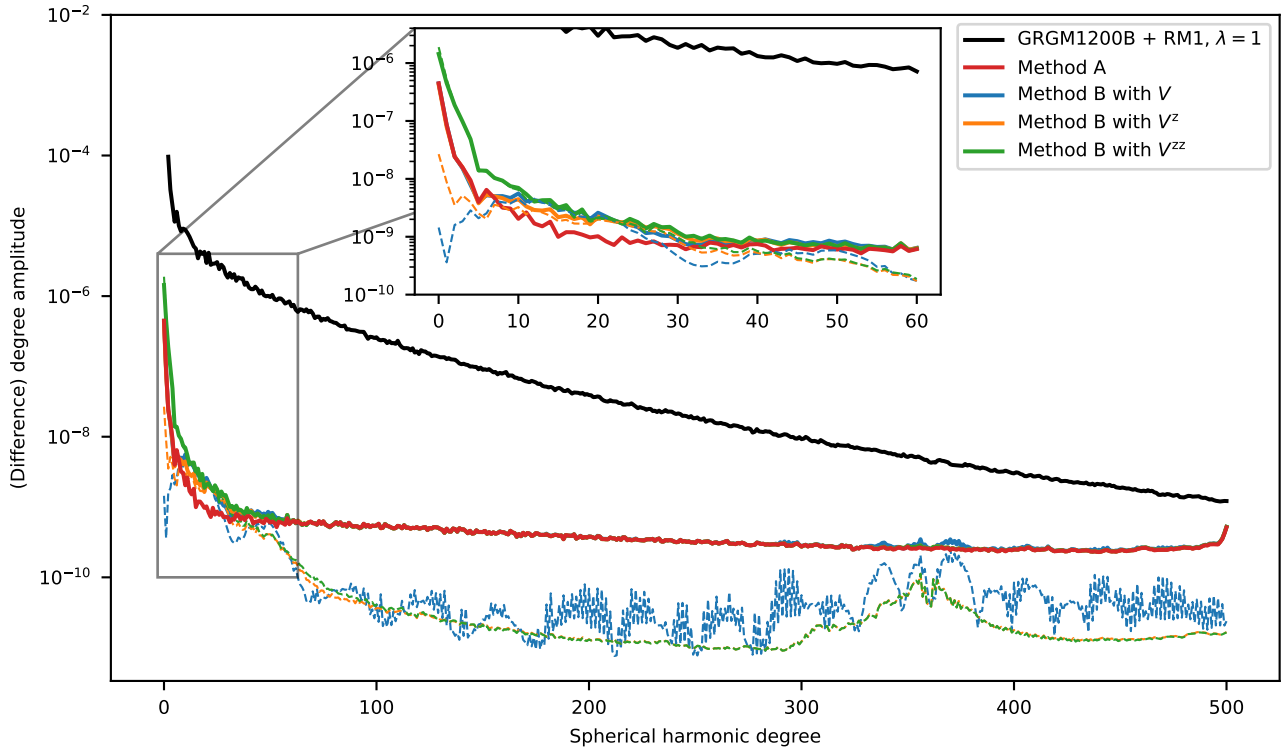

Figure S9. Low-frequency RTM corrections from the methods A and B (all shown in thick solid lines). For a comparison, the GRAIL gravitational signal from GRGM1200B + RM1, $\lambda = 1$ is shown for degrees 2 – 500 (degrees 0 and 1 are omitted in this case in order not to overload the figure). The thin dashed lines show difference degree amplitudes between the methods A and B. The GRGM1200B + RM1, $\lambda = 1$ model was rescaled to our circumscribing sphere to make it consistent with the other signals. All models use the same GM, which is here taken from GRGM1200B + RM1, $\lambda = 1$.

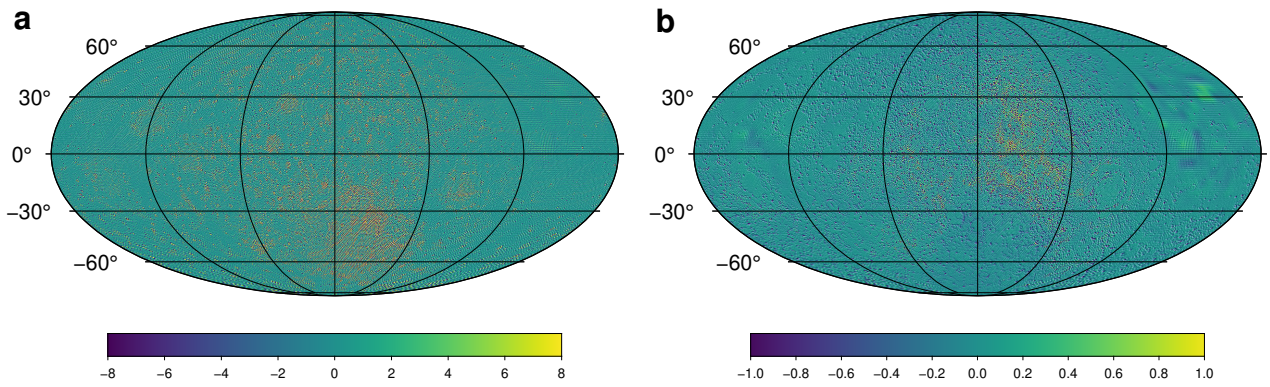

Figure S10. Low-frequency RTM correction for V^{z} in mGal at the lunar surface (a) and on the circumscribing sphere (b). The statistics of the low-frequency correction (min/max/mean/root mean square, all in mGal) are −9.5e+01/7.7e+01/−7.2e−02/4.1e+00 for the lunar topography and −7.3e+00/7.3e+00/−7.4e−02/3.0e−01 for the circumscribing sphere. The maps are centered at the 180° meridian.

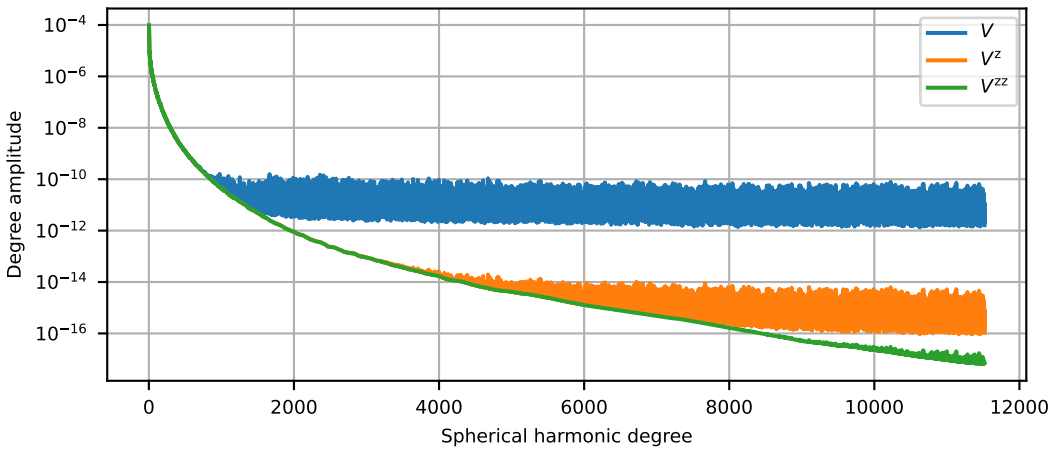

Figure S11. Degree amplitudes obtained by harmonically analyzing V, V^{z} and V^{zz} on the circumscribing sphere. Harmonic degrees 0 and 1 are omitted for visualization purposes.

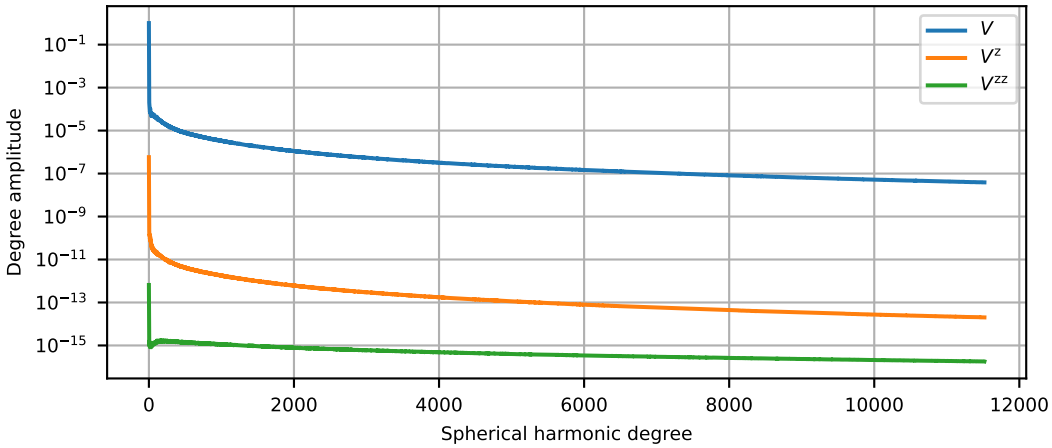

Figure S12. Spectrum of the V (dimensionless), V^{z} (units m^{-1}) and V^{zz} (units m^{-2}) surface grids assuming the data are signals on the sphere of the radius 1749 km. All coefficients are normalized by the GM and $R = 1749$ km constants. This time, the Meissl scheme is not applied for V^{z} and V^{zz}.

Table S2. Errors of V^{GRAIL} (Equation 4) obtained by error propagation of GRGM1200B up to degree 500 onto 1920 × 3840 grids (5.625 arcmin) residing at the topography level and on the circumscribing sphere. The evaluation points are a subset of LGM2026 grid points.

	Topography			Circumscribing sphere		
Quantity	min	max	90th percentile	min	max	90th percentile
V [m^2 s^{-2}]	1.6e-04	9.5e-02	1.6e-02	6.5e-05	1.9e-03	5.5e-04
V^{x} [mGal]	2.3e-03	1.7e+00	2.5e-01	4.0e-04	3.9e-02	8.3e-03
V^{y} [mGal]	2.7e-03	1.9e+00	3.4e-01	4.4e-04	3.2e-02	1.1e-02
V^{z} [mGal]	3.7e-03	2.6e+00	4.2e-01	6.9e-04	4.6e-02	1.4e-02
V^{xx} [E]	5.7e-03	3.8e+00	5.7e-01	9.2e-04	8.8e-02	1.8e-02
V^{xy} [E]	3.5e-03	2.4e+00	3.9e-01	6.5e-04	3.5e-02	1.2e-02
V^{xz} [E]	6.4e-03	4.6e+00	6.9e-01	1.1e-03	9.8e-02	2.1e-02
V^{yy} [E]	6.8e-03	4.6e+00	8.3e-01	1.0e-03	7.4e-02	2.5e-02
V^{yz} [E]	7.7e-03	5.4e+00	9.1e-01	1.2e-03	8.1e-02	2.8e-02
V^{zz} [E]	1.0e-02	7.0e+00	1.1e+00	2.0e-03	1.1e-01	3.5e-02

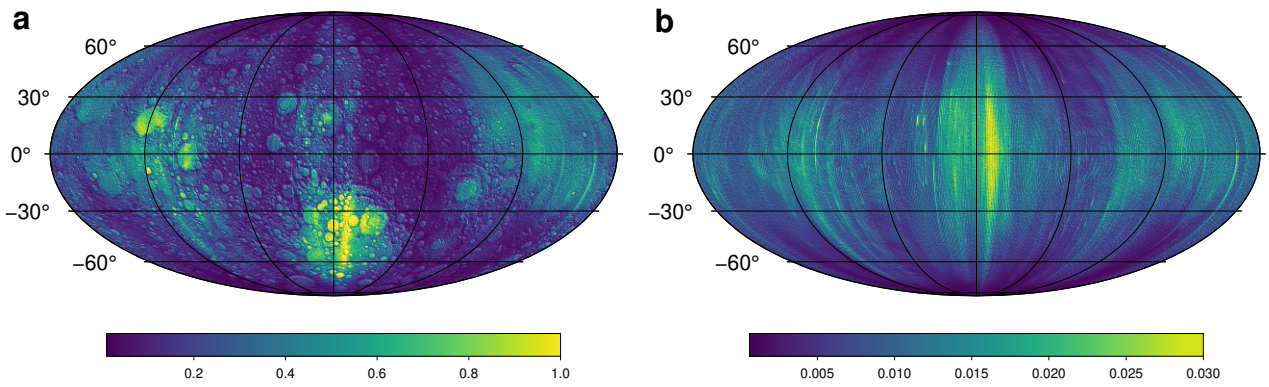

Figure S13. Errors of $V^{z,\mathrm{GRAIL}}$ in mGal at the topography (a) and on the circumscribing sphere (b). The maps are centered at the 180° meridian.

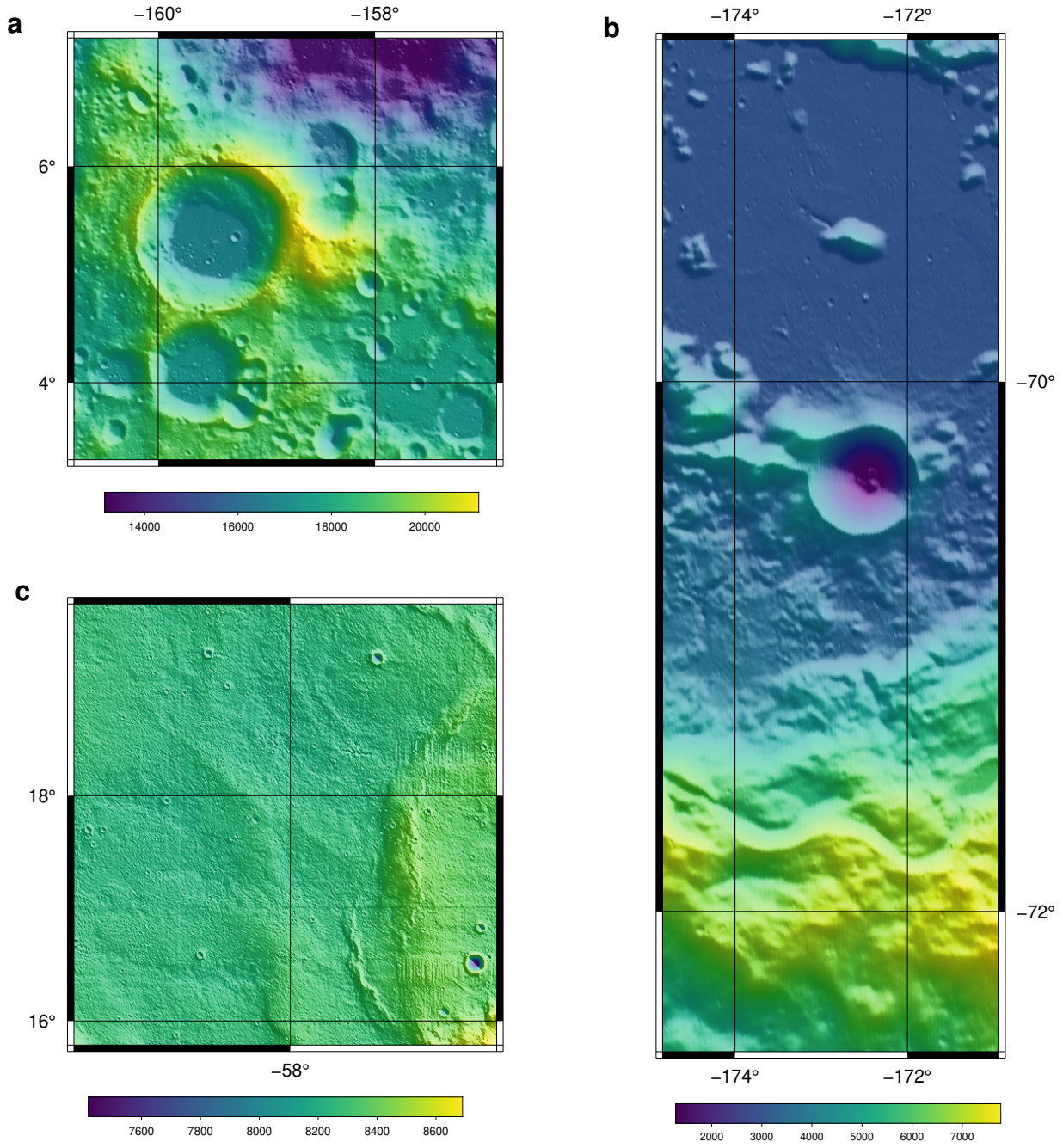

Figure S14. Topography (m) over study areas for experiments from Text S5.3.1 and Text S5.4: area 1 (a), area 2 (b) and area 3 (c). The resolution of the maps is 128 PPD, but the evaluation points were downsampled by a factor of 10 in these experiments. The grids of the gravitating masses were used in their original resolution of 128 PPD.

Table S3. Propagation of LDEM128 errors to gravitational quantities for spatial-domain gravity-forward modeling in the study area 1 (highlands near the equator, the highest lunar topography point included). The study area is given by 50×50 point grid with the 0.078125° spacing covering the latitudes from 3.4° to 7.2° and longitudes from 199.2° to 203.1° (subset of LGM2026 grid points). Shown are the minimum standard deviations, the maximum standard deviations and the 90th percentile.

Quantity	min	max	90th percentile
V [m^2 s^{-2}]	9.8e-02	2.0e-01	1.8e-01
V^x [mGal]	2.0e-01	5.1e-01	3.5e-01
V^y [mGal]	2.0e-01	5.2e-01	3.5e-01
V^z [mGal]	1.4e-01	1.6e+00	7.7e-01
V^{xx} [E]	1.6e+01	7.1e+01	4.7e+01
V^{xy} [E]	6.3e+00	1.5e+01	1.1e+01
V^{xz} [E]	1.2e+01	8.2e+01	2.0e+01
V^{yy} [E]	1.6e+01	6.8e+01	4.7e+01
V^{yz} [E]	1.2e+01	6.1e+01	1.9e+01
V^{zz} [E]	3.0e+01	1.2e+02	7.5e+01

Table S4. The same as Table S3 but for the study area 2 (the South Pole–Aitken basin, the lowest lunar topography point included) given by 50×50 point grid with the 0.078125° spacing covering the latitudes from −68.6° to −72.4° and longitudes from 185.2° to 189.0° (subset of LGM2026 grid points)

Quantity	min	max	90th percentile
V [m^2 s^{-2}]	7.3e-03	7.6e-02	5.8e-02
V^{x} [mGal]	7.5e-02	2.1e-01	1.5e-01
V^{y} [mGal]	1.8e-01	6.4e-01	5.0e-01
V^{z} [mGal]	1.4e-01	1.5e+00	1.0e+00
V^{xx} [E]	1.1e+01	3.6e+01	2.5e+01
V^{xy} [E]	2.8e+00	1.2e+01	7.2e+00
V^{xz} [E]	8.7e-01	4.1e+01	2.2e+01
V^{yy} [E]	2.8e+01	3.2e+02	2.0e+02
V^{yz} [E]	1.6e+01	2.1e+02	8.8e+01
V^{zz} [E]	2.9e+01	2.9e+02	2.0e+02

Table S5. The same as Table S3 but for the study area 3 (Oceanus Procellarum, flat topography) given by 50×50 point grid with the 0.078125° spacing covering the latitudes from 15.9° to 19.7° and longitudes from 300.0° to 303.8° (subset of LGM2026 grid points)

Quantity	min	max	90th percentile
V [m^2 s^{-2}]	6.1e-02	1.0e-01	8.6e-02
V^{x} [mGal]	2.0e-01	3.8e-01	3.3e-01
V^{y} [mGal]	1.8e-01	3.9e-01	3.5e-01
V^{z} [mGal]	5.2e-01	1.6e+00	1.0e+00
V^{xx} [E]	1.4e+01	7.5e+01	6.3e+01
V^{xy} [E]	5.2e+00	1.1e+01	9.9e+00
V^{xz} [E]	3.1e+00	5.0e+01	6.1e+00
V^{yy} [E]	1.2e+01	7.9e+01	6.9e+01
V^{yz} [E]	4.0e+00	6.0e+01	7.6e+00
V^{zz} [E]	2.4e+01	1.4e+02	1.2e+02

Table S6. Impact of the Gauss–Legendre quadrature orders on the accuracy of spatial-domain gravity-forward modeling. The orders are here denoted as $O_1/O_2/O_3/O_4$, where the order O_1 is used for tesseroids up the to spherical distance $\psi < 0.3°$ from the evaluation points, O_2 is used for $0.3° \leq \psi < 0.5°$, O_3 is used for $0.5° \leq \psi < 3°$ and O_4 is used for $3° \leq \psi < 10°$ (see also Text S2.1). The table reports statistics of the discrepancies between the solution with 11/5/3/2 (used in the LGM2026 development) and 2 higher-order solutions. The max column shows the maximum error in absolute value, STD stands for the standard deviation and the 90th percentile is shown for the absolute value of the discrepancies. The statistics are reported for the area 1 from Text S5.3.1.

	Gauss–Legendre quadrature 15/9/7/6				Gauss–Legendre quadrature 17/11/9/8			
Quantity	max	mean	STD	90th percentile	max	mean	STD	90th percentile
V [m^2 s^{-2}]	8.6e-03	-5.6e-03	1.9e-03	7.6e-03	8.6e-03	-5.6e-03	1.9e-03	7.5e-03
V^x [mGal]	3.5e+00	-9.0e-02	4.8e-01	7.8e-01	4.0e+00	-1.2e-01	6.5e-01	1.1e+00
V^y [mGal]	3.2e+00	1.7e-02	4.9e-01	7.3e-01	3.7e+00	2.4e-02	6.6e-01	1.0e+00
V^z [mGal]	1.8e+00	-1.5e-01	1.9e-01	3.8e-01	1.7e+00	-8.2e-02	1.9e-01	3.1e-01
V^{xx} [E]	5.5e+02	1.0e+01	3.3e+01	3.3e+01	6.7e+02	2.5e+01	5.4e+01	7.4e+01
V^{xy} [E]	9.1e+01	-1.5e+00	1.7e+01	2.9e+01	9.0e+01	-1.6e+00	1.9e+01	3.2e+01
V^{xz} [E]	4.3e+02	2.1e+01	1.0e+02	1.8e+02	4.4e+02	2.5e+01	1.2e+02	2.2e+02
V^{yy} [E]	4.8e+02	9.9e+00	3.5e+01	2.8e+01	6.1e+02	2.4e+01	5.8e+01	6.2e+01
V^{yz} [E]	4.6e+02	-4.3e+00	1.0e+02	1.7e+02	5.0e+02	-5.2e+00	1.2e+02	2.2e+02
V^{zz} [E]	5.4e+02	-2.0e+01	4.8e+01	6.5e+01	6.7e+02	-4.9e+01	7.9e+01	1.5e+02

Table S7. The same as Table S6 but for the study area 2.

	Gauss–Legendre quadrature 15/9/7/6				Gauss–Legendre quadrature 17/11/9/8			
Quantity	max	mean	STD	90th percentile	max	mean	STD	90th percentile
V [m^2 s^{-2}]	2.7e-04	-1.4e-05	2.9e-05	3.8e-05	2.8e-04	-1.5e-05	3.0e-05	4.0e-05
V^{x} [mGal]	4.9e-01	1.1e-02	5.9e-02	8.8e-02	4.9e-01	1.1e-02	5.6e-02	7.8e-02
V^{y} [mGal]	8.6e-01	-4.6e-03	1.1e-01	1.7e-01	1.2e+00	-7.7e-03	1.2e-01	2.0e-01
V^{z} [mGal]	7.5e-01	2.4e-02	9.4e-02	1.3e-01	8.2e-01	2.8e-02	1.0e-01	1.4e-01
V^{xx} [E]	1.3e+02	-3.2e+00	1.6e+01	2.4e+01	1.3e+02	-4.2e+00	1.6e+01	2.2e+01
V^{xy} [E]	3.0e+01	-4.5e-03	2.8e+00	3.1e+00	3.0e+01	4.2e-02	2.7e+00	3.1e+00
V^{xz} [E]	1.3e+02	-2.7e+00	1.9e+01	2.7e+01	1.2e+02	-2.1e+00	1.9e+01	2.9e+01
V^{yy} [E]	3.6e+02	1.6e+01	4.8e+01	6.0e+01	4.0e+02	1.9e+01	5.1e+01	7.6e+01
V^{yz} [E]	5.3e+02	4.3e+00	5.9e+01	9.5e+01	5.5e+02	6.4e+00	7.2e+01	1.2e+02
V^{zz} [E]	3.6e+02	-1.2e+01	4.7e+01	5.9e+01	4.0e+02	-1.5e+01	5.0e+01	7.2e+01

Table S8. The same as Table S6 but for the study area 3.

	Gauss–Legendre quadrature 15/9/7/6				Gauss–Legendre quadrature 17/11/9/8			
Quantity	max	mean	STD	90th percentile	max	mean	STD	90th percentile
V [m^2 s^{-2}]	5.3e-04	-3.4e-05	2.2e-05	4.2e-05	6.4e-04	-3.5e-05	2.6e-05	4.0e-05
V^{x} [mGal]	3.9e-01	-1.0e-03	2.7e-02	2.5e-02	4.0e-01	-1.2e-03	2.7e-02	2.5e-02
V^{y} [mGal]	4.7e-01	-2.4e-03	3.2e-02	3.0e-02	4.3e-01	-2.1e-03	3.1e-02	3.1e-02
V^{z} [mGal]	1.5e+00	4.3e-03	7.0e-02	1.1e-02	1.5e+00	5.1e-03	7.6e-02	2.0e-02
V^{xx} [E]	1.2e+02	5.9e-01	7.7e+00	5.9e+00	1.3e+02	5.0e-01	8.1e+00	7.3e+00
V^{xy} [E]	4.3e+01	-4.6e-04	1.7e+00	6.2e-01	4.1e+01	1.1e-03	1.6e+00	5.6e-01
V^{xz} [E]	1.9e+02	2.7e-01	6.0e+00	3.6e+00	2.1e+02	2.7e-01	6.6e+00	2.9e+00
V^{yy} [E]	1.4e+02	8.4e-01	8.3e+00	5.9e+00	1.4e+02	8.0e-01	8.5e+00	7.6e+00
V^{yz} [E]	1.7e+02	1.1e-01	6.8e+00	5.0e+00	2.1e+02	-1.6e-02	7.7e+00	4.3e+00
V^{zz} [E]	2.4e+02	-1.4e+00	1.5e+01	1.0e+01	2.5e+02	-1.3e+00	1.5e+01	1.3e+01

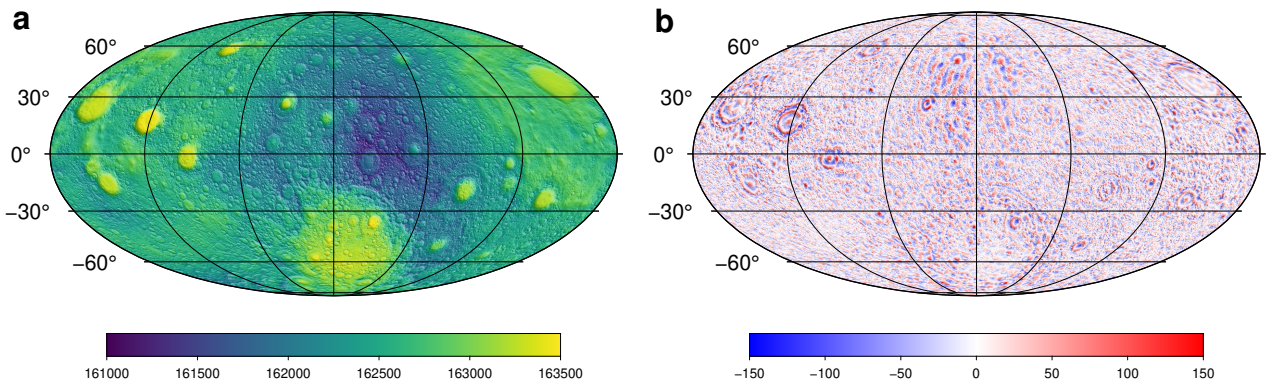

Figure S15. (a) Gravitational acceleration from LGM2026 (block averaged to the $0.05° \times 0.05°$ resolution to match LGM2011) and (b) its difference with respect to LGM2011. Before the comparison, the centrifugal acceleration was removed from the surface gravity of LGM2011 to get the gravitational acceleration. The statistics of the differences (min/max/mean/standard deviation) are $-220.3/203.2/0.5/22.8$. All values in mGal.

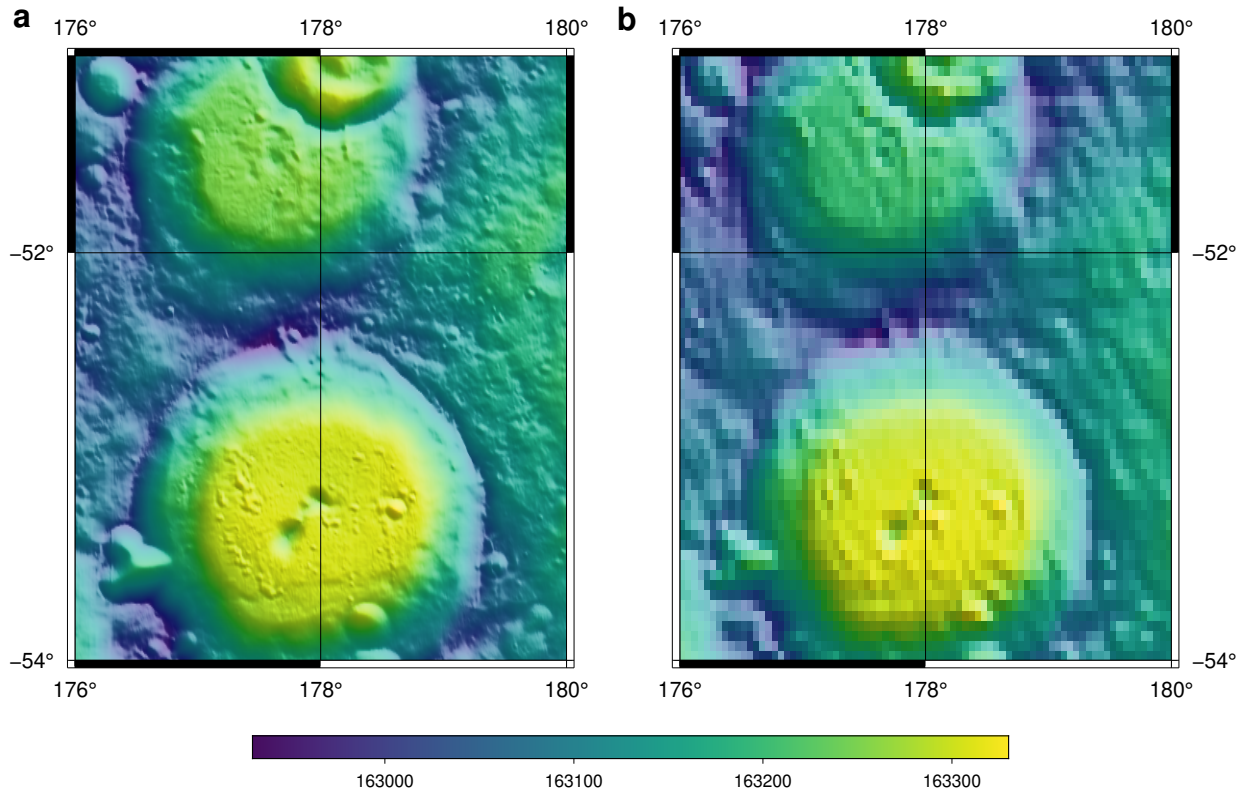

Figure S16. Gravitational acceleration in mGal from LGM2026 (a) and LGM2011 (b). Both models are shown in their full resolution. The centrifugal acceleration was removed from LGM2011. LGM2026 is shown in the Moon's principal axis coordinate system and LGM2011 is shown in the Mean-Earth/Polar-Axis coordinate system.

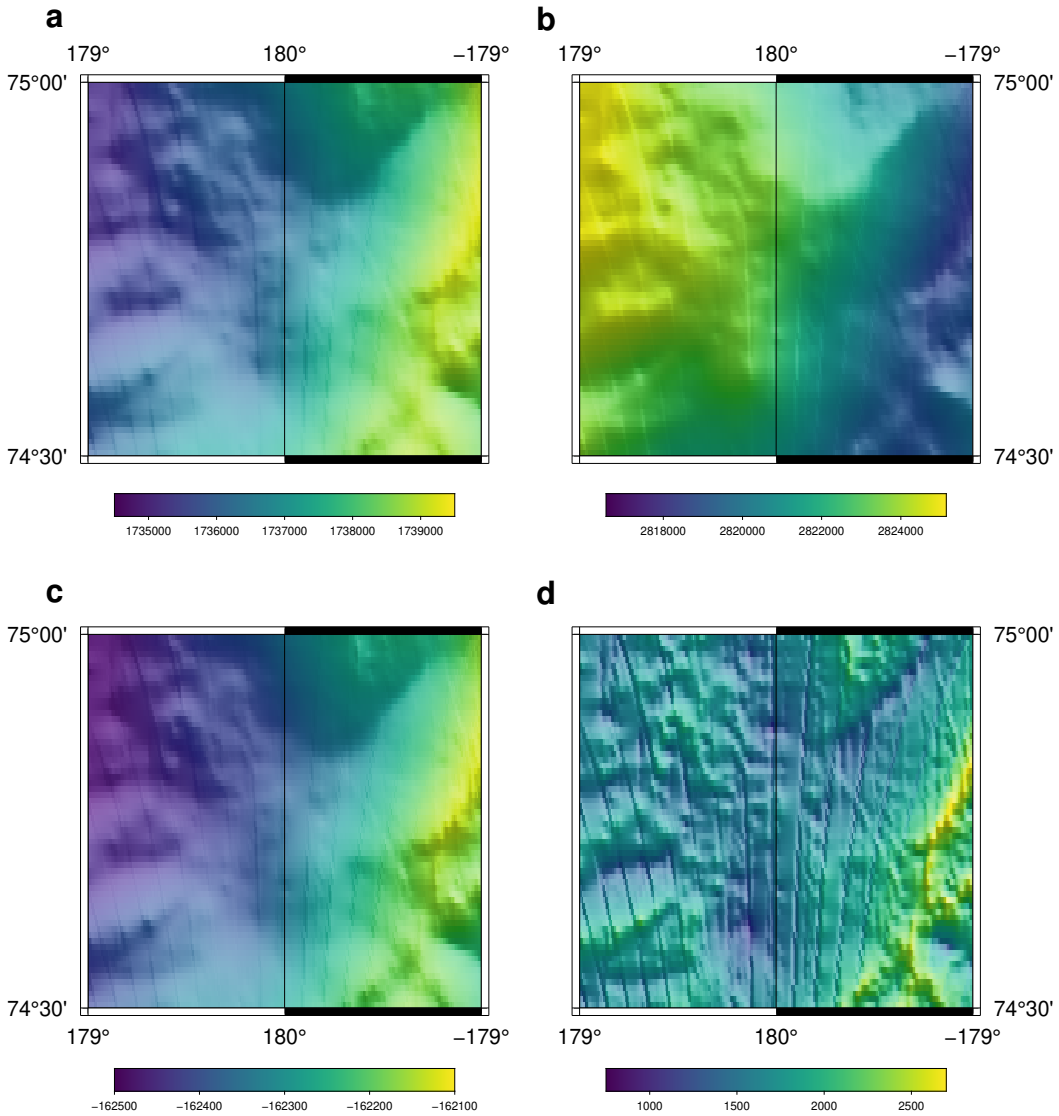

Figure S17. Artifacts in LDEM128, which propagated into LGM2026. Spherical radius of the lunar topography in meters (a), the gravitational potential in $m^2\ s^{-2}$ (b), the V^z element of the gravitational vector in mGal (c) and the V^{zz} element of the gravitational tensor in E (d).